Applications of Linear and Nonlinear Robustness Analysis Techniques to the F/A-18 Flight Control Laws

Abhijit Chakraborty * and Peter Seiler † and Gary J. Balas‡

Department of Aerospace Engineering & Mechanics, University of Minnesota , Minneapolis, MN, 55455, USA

The F/A-18 Hornet aircraft with the original flight control law exhibited an out-of-control phenomenon known as the falling leaf mode. Several aircraft were lost due to the falling leaf mode and which led NAVAIR and Boeing to redesign the flight control law. The revised flight control law successfully suppressed the falling leaf mode during flight tests with aggressive maneuvers. This paper compares the robustness of the original (baseline) and revised control laws using linear analyses, Monte Carlo simulations, and nonlinear region-of-attraction analyses. The linear analyses indicate the revised controller only marginally improves the closed-loop robustness while the nonlinear analyses indicate a substantial improvement in robustness over the baseline controller. This example demonstrates the potential for nonlinear analyses to detect out-of-control phenomenon that are not evident from linear analyses.

Nomenclature

α	Angle-of-attack, rad
β	Sideslip Angle, rad
V_T	Velocity, ft/s
p	Roll rate, rad/s
q	Pitch rate, rad/s
r	Yaw rate, rad/s
ϕ	Bank angle, rad
θ	Pitch angle, rad
ψ	Yaw angle, rad
T	Thrust, lbf
ρ	Density, slugs/ft^3
$\bar{q}$	$\frac{1}{2}\rho V_T^2$: Dynamic pressure
V	Lyapunov Function
m	Mass, slugs
IC	Initial Condition

I.   Introduction

The US Navy F/A-18 A/B/C/D Hornet aircraft with the original baseline flight control law experienced a number of out-of-control flight departures since the early 1980's. Many of these incidents have been described as a falling leaf motion of the aircraft.[1] The falling leaf motion has been studied extensively to investigate the conditions that lead to this behavior. The complex dynamics of the falling leaf motion and lack of flight data from the departure events pose a challenge in studying this motion. An extensive revision of the baseline control law was performed by NAVAIR and Boeing in 2001 to suppress departure phenomenon, improve

---

*Graduate Research Assistant: chakrab@aem.umn.edu.

†Senior Research Associate: seile017@umn.edu.

‡Professor: balas@aem.umn.edu.

American Institute of Aeronautics and Astronautics

maneuvering performance and to expand the flight envelope.[1] The revised control law was implemented on the F/A-18 E/F Super Hornet aircraft after successful flight tests. These flight tests included aggressive maneuvers that demonstrated successful suppression of the falling leaf motion by the revised control law.

It is of practical interest to compare the robustness of the baseline and revised flight controllers. One objective of this paper is to use linear analyses, Monte Carlo simulations, and nonlinear region of attraction analyses to compare the robustness guarantees of each of the design. Region-of-attraction analysis for nonlinear systems provides a guaranteed stability region using Lyapunov theory and recent results in sum-of-squares optimization.[2-6] This is complementary to the use of Monte Carlo simulations to search for unstable trajectories. The sums-of-squares stability analysis has previously been applied to simple examples,[2-6] though this is the first application of these techniques to an actual industry flight control problem. The second objective is to use the nonlinear region-of-attraction technique to analyze and draw conclusions about the F/A-18 aircraft flight control system. Nonlinear analysis is necessary as the falling leaf motion is due to nonlinearities in the aircraft dynamics and cannot be replicated in simulation by linear models. This makes the falling leaf motion a particularly interesting example for the application of nonlinear robustness analysis techniques.

The remainder of the paper has the following outline. Section II describes the characteristics of the falling leaf motion. Section III provides a brief description of the F/A-18 aircraft including its aerodynamic characteristics and equations of motion. The baseline and revised flight control laws are described in Section IV. Section V provides a comparison of the closed-loop robustness properties with the baseline and revised flight control laws. This section includes both the linear and nonlinear analyses for each control law. A summary of results and comparisons between linear robustness and nonlinear analyses techniques is also presented in Section V. Finally a brief conclusion is given in Section VI. All data required to reproduce the results presented in this paper are provided in the Appendices.

II. Falling Leaf Motion

The falling leaf motion of an aircraft can be characterized as large, coupled out-of-control oscillations in the roll (p) and yaw (r) direction combined with large fluctuations in angle-of-attack (α) and sideslip (β).[1,7] Figure 1 shows the main characteristics of the falling leaf motion.[1,7] This out-of-control mode exhibits periodic in-phase roll and yaw rates with large amplitude fluctuations about small or zero mean. The roll and yaw rate generation is mainly due to the large sideslip oscillation. During large sideslip and angle-of-attack motion, the dihedral effect (roll caused by sideslip) of the aircraft wings becomes extremely large and the directional stability becomes unstable. The like-signs of these two values are responsible for the in-phase motion. The roll rate motion can easily reach up to $\pm 120°/s$, while the yaw rate motion can fluctuate around $\pm 50°/s$. During this motion, the value of angle-of-attack can reach up to $\pm 70°$ with sideslip oscillations between $\pm 40°$.[7] The required aerodynamic nose-down pitching moment is exceeded by the pitch rate generation due to the inertial coupling of the in-phase roll and yaw rates. The reduction in pitching moment is followed by a reduction in normal force, eventually causing a loss of lift in the aircraft. A distinguishing feature of the falling leaf motion is that α vs. β plot produces a mushroom shape curve as seen in Figure 1. For more details on the falling leaf motion, readers are encouraged to refer to the papers by Jaramillo & Ralston[7] and Heller, David & Holmberg.[1]

III. F/A-18 Aircraft Description and Model Development

This section contains a brief description of the F/A-18 Hornet including the physical parameters and the aerodynamic characteristics of the aircraft. More information can be found in the report by Buttrill, Arbuckle, and Hoffler.[8] A full six degree-of-freedom (DOF) nonlinear model of the F/A-18 Hornet dynamics is presented in Appendix A. This full model is not directly used in any of the analyses presented in this paper and is only included for completeness. Each of the analyses presented in this paper uses a slightly different approximated model derived from this full 6 DOF model. To avoid confusion, it is worth summarizing the various models which will be used. A six state, cubic polynomial model, presented in Appendix B, is appropriate for the analysis of roll-coupled maneuvers. This cubic polynomial model was used to generate the falling leaf simulations shown in Figure 1 and for linearization about trim points. It was also used for linearization around eight different trim points corresponding to steady and unsteady turning maneuvers. These models are described further in Section III.E. The resulting linear state space models are used to
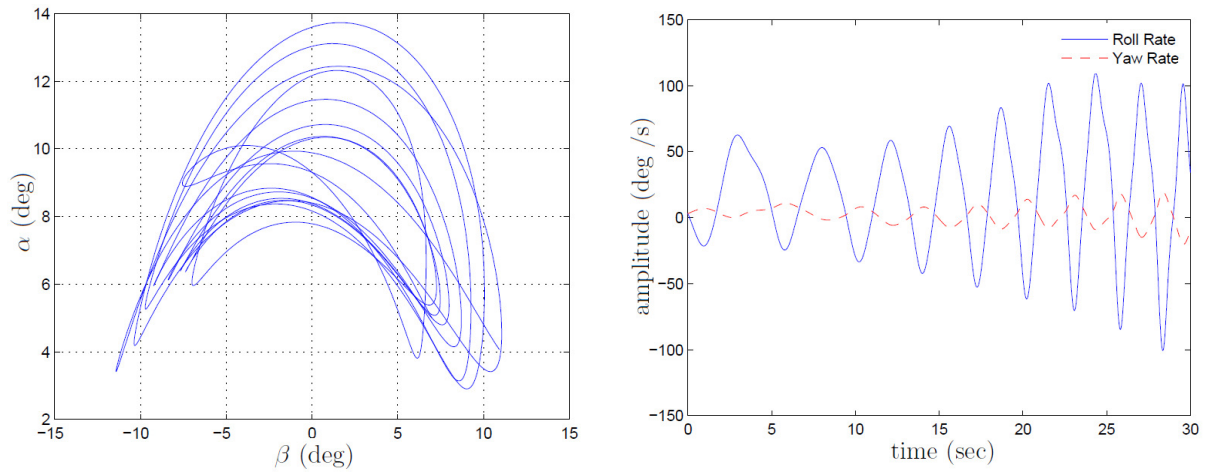
American Institute of Aeronautics and Astronautics

Figure 1. Characteristic Behavior of Falling Leaf Motion

perform the linear robustness analysis in Section V.A. One of these open loop linear plant (Plant 4 in Table 3) is provided in Appendix C. The state space realizations of both the baseline and revised control laws are provided in Appendix D. For either control law, the closed loop system can be constructed by placing the linear control law in Appendix D in negative feedback around the appropriate linear model. Feeding back the baseline or revised control law around the cubic polynomial model results in a model that is a rational function of the states. The nonlinear region-of-attraction analysis in Section V.B.2 requires the closed-loop system dynamics be described by a polynomial function of the states. To derive a polynomial model for the region of attraction analysis, linear least square and Taylor series approximation are used to approximate the closed-loop systems as cubic polynomial functions of the states. These polynomial models are provided in Appendix E. Figure 2 shows the steps used to derive the F/A-18 aircraft models used in this paper.
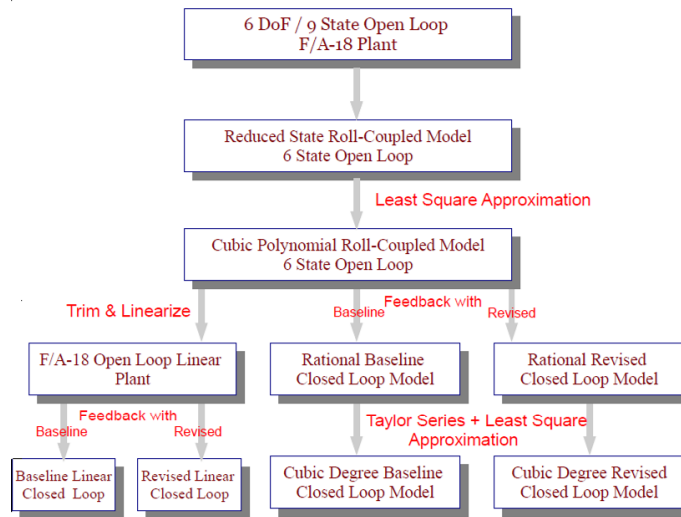

Figure 2. Steps for F/A-18 Model Reduction

As we proceed through the various analyses, the model being used in each case will be explicitly stated. The polynomial model captures the characteristics of the full 6 DOF model. However, the closed-loop polynomial model has not been able to reproduce the mushroom shape curve for α-β plot, as seen in Figure 1.

American Institute of Aeronautics and Astronautics

A. Physical Parameters

Figure 3. F/A-18 Hornet

The F/A-18 Hornet aircraft, Figure 3[a], is a high performance, twin engine fighter aircraft built by the McDonnell Douglas (currently known as the 'Boeing') Corporation. Each engine is a General Electric, F404-GE-400 rated at 16,100-lbf of static thrust at sea level. The aircraft features a low sweep trapezoidal wing planform with 400 ft^2 area and twin vertical tails.[8] Table 1 lists the aerodynamic reference and physical parameters of the aircraft.

Table 1. Aircraft Parameters

Wing Area, S_{ref}	400 ft^2
Mean Aerodynamic Chord ($\bar{c}$)	11.52 ft
Wing Span, b_{ref}	37.42 ft
Mass, m	1034.5 slugs
I_{xx}	23000 slug-ft^2
I_{yy}	151293 slug-ft^2
I_{zz}	169945 slug-ft^2
I_{xz}	-2971 slug-ft^2

B. Control Surfaces

The conventional F/A-18 Hornet aircraft has five pairs of control surfaces: stabilators, rudders, ailerons, leading edge flaps, and trailing edge flaps. However, only the symmetric stabilator, differential aileron and differential rudder are considered as control effectors for the analyses performed in this paper. Longitudinal control or pitch control is provided by the symmetric deflection of the stabilators. Deflection of differential ailerons is used to control the roll or lateral direction, while differential deflection of rudders provide directional or yaw control. The actuation systems for these primary controls are modeled as first order lags. Table 2 provides the mathematical models of the actuators and their deflection and rate limits.[8] However, the actuators' dynamics and rate/position limits are neglected for all analyses. Their values are only included for completeness.

Table 2. Control Surface and Actuator Configuration

Actuator	Rate Limit	Position Limit	Model
Stabilator, δ_{stab}	$\pm 40°$/s	$-24°,+10.5°$	$\frac{30}{s+30}$
Aileron, δ_{ail}	$\pm 100°$/s	$-25°,+45°$	$\frac{48}{s+48}$
Rudder, δ_{rud}	$\pm 61°$/s	$-30°,+30°$	$\frac{40}{s+40}$

---

[a]Pictures taken from http://www.dfrc.nasa.gov/Gallery/Photo/F-18Chase/Large/EC96-43830-11.jpg

C.   Equations of Motion & Aerodynamic Model

The conventional aircraft equations of motion described in Stengel,[9] Cook,[10] and Napolitano and Spagnuolo[11] are primarily driven by the aerodynamic forces and moments acting on the aircraft. In this paper, we follow the notation used in the report by Napolitano and Spagnuolo.[11] The equations of motion for the 6 DOF full model are presented in the Appendix A. The two aerodynamic angles, angle-of-attack (α) and sideslip angle (β), are needed to specify the aerodynamic forces and moments. These aerodynamic forces and moments also depend on the angular rates and the deflection of the control surfaces. The longitudinal coefficients (lift, drag, and pitching moment) primarily depend on the angle-of-attack (α); in the lateral directional coefficients (roll, yaw, and sideforce), sideslip angle (β) is equally as important as α.[12] Many flight experiments have been performed to estimate the stability and control derivatives of the F/A-18 High Alpha Research Vehicle (HARV).[13–16] The F/A-18 HARV has similar aerodynamic characteristics as the F/A-18 Hornet[17] with the exception of the F/A-18 HARV having thrust vectoring control. Hence, we will use the F/A-18 HARV aerodynamic data to represent the F/A-18 aircraft in all models that are presented in this paper. The aerodynamic model for the full six degree-of-freedom model is presented in the Appendix A.

D.   Reduced Equations of Motion

The nonlinear region of attraction analysis[3] requires the aircraft dynamics to be described by a polynomial model. The computational burden of the analysis also restricts the polynomial degree to be less than or equal to 3. Hence, a six state cubic polynomial model of the F/A-18 aircraft for roll-coupled maneuvers[18] is used in this paper for performing all the analyses. The reduced (open loop cubic polynomial) equations of motion are presented in the Appendix B.

The polynomial model described in the Appendix B captures the characteristics of the full 6 DOF model presented in Appendix A. During this OCF motion, the velocity is usually on the order of 250 ft/s.[7] In this paper, the velocity is assumed to be constant, and equal to 250 ft/s. Aggressive maneuvers, like bank turn, are more likely to put the aircraft in the falling leaf motion compared to straight and level flight. Hence, we consider a steady bank turn maneuver of the aircraft with zero climb rate ($\dot{\theta} = 0$). This assumption allows the pitch angle (θ) and yaw angle (ψ) to be ignored, resulting in a six state model. Thrust effects in the sideslip direction are also neglected. Small angle approximations are used for the trigonometric terms in the full 6 DOF model to derive a polynomial representation of the aircraft dynamics. Finally, we perform least squares fit of the aerodynamic data over a gridded α - β space of $-20° \leq \beta \leq 20°$, and $-10° \leq \alpha \leq 40°$ to restrict the description of the dynamics up to cubic degree.

E.   Formulation of Linear Models

The cubic polynomial model, presented in Appendix B, is linearized around steady ($\beta = 0$) and unsteady ($\beta = 10^o$) turning maneuvers for different bank angles (ϕ). Steady bank turn is a usual maneuver for any aircraft. However, wind disturbances or any upset conditions can force the aircraft to perform unsteady bank turn maneuvers. Hence, we will consider both scenarios. Aggressive maneuvers, like large bank turn (i.e, $\phi = 60^o$), are more likely to put the aircraft into the falling leaf motion compared to straight and level flight. Longitudinal and lateral direction become highly coupled during such maneuvers. Hence, linearization around such maneuvers will result in linear models which may be well suited to capture the coupling effect of the aircraft which is one of the important causes for initiating the falling leaf motion.[7] It is of considerable interest to perform linear robustness comparison between the baseline and revised flight control law. The operating points for formulating the linear models are presented in Table 3. All the linear aircraft models are trimmed around the flight condition of: $V_T = 250$ ft/s, altitude $= 25,000$ ft, and $\alpha = 26^o$. We will perform the nonlinear analysis around the trim condition listed for Plant 4 in Table 3. Only Plant 4 and Plant 8 are considered for loopmargin analysis. In addition, all eight plants, mentioned in Table 3, are used to perform the linear robustness (μ) analysis as presented in Section V.A.

IV.   Control Law Design

This section provides an overview of both the baseline and revised control laws. In both cases, the control laws are divided into three channels: longitudinal, lateral, and directional.

American Institute of Aeronautics and Astronautics

Table 3. Trim Values around $V_T = 250 \frac{ft}{s}$ altitude $=25,000$ ft, and $\alpha = 26^o$

State/Input	Plant 1	Plant 2	Plant 3	Plant 4	Plant 5	Plant 6	Plant 7	Plant 8
Sideslip, β	0°	0°	0°	0°	10°	10°	10°	10°
Bank Angle, ϕ	0°	25°	45°	60°	0°	25°	45°	60°
Roll Rate, p	0°/s	0°/s	0°/s	0°/s	0°/s	0°/s	0°/s	0°/s
Yaw Rate, r	0°/s	3.20°/s	5.78°/s	7.70°/s	0.069°/s	3.28°/s	5.84°/s	7.77°/s
Pitch Rate, q	0°/s	0°/s	0°/s	0°/s	0°/s	0°/s	0°/s	0°/s
δ_{Stab}	-21.78°	-21.78°	-21.78°	-21.78°	-21.78°	-21.78°	-21.78°	-21.78°
δ_{Ail}	0°	0.31°	0.56°	0.75°	19.68°	19.98°	20.24°	20.42°
δ_{Rud}	0°	-2.37°	-4.27°	-5.69°	3.32°	0.96°	-0.94°	-2.36°
T (lbf)	36464	36464	36464	36464	36464	36464	36464	36464

A. Baseline Control Law

Figure 4 shows the control law architecture for the baseline control laws used for analysis in this paper. The baseline controller structure for the F/A-18 aircraft closely follows the *Control Augmentation System (CAS)* presented in the report by Buttrill, Arbuckle, and Hoffler.[8] The actuator ($A_{stab}, A_{rud}, A_{ail}$) dynamics, presented in Table 2, are neglected for analysis purposes, i.e. $A_{stab} = A_{rud} = A_{ail} = 1$. Any differences between the control structure presented here and in the report by Buttrill, Arbuckle, and Hoffler[8] is described in the following sections.
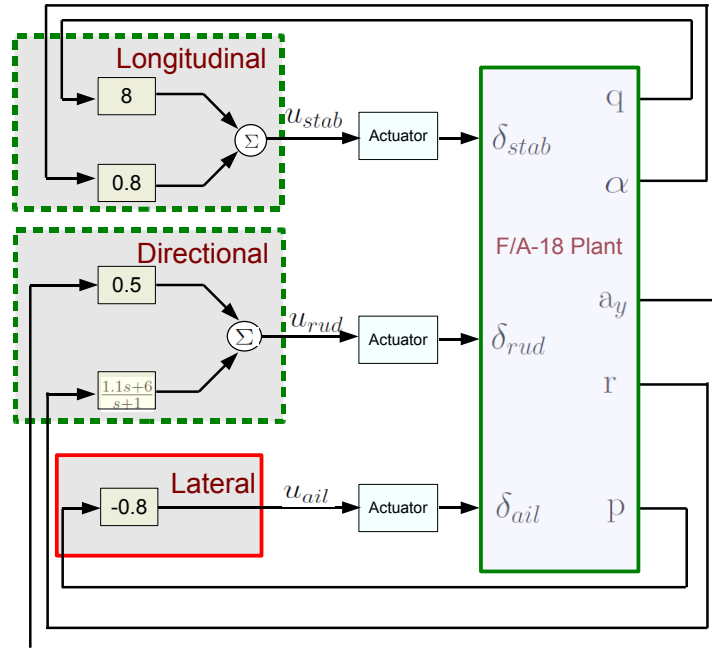

Figure 4. F/A-18 Baseline Flight Control Law

1. Longitudinal Control

The longitudinal baseline control design for the F/A-18 aircraft includes angle-of-attack (α in rad), normal acceleration (a_n in g), and pitch rate (q in rad/s) feedback. The angle-of-attack feedback is used to stabilize an unstable short-period mode that occurs during low speed, high angle-of-attack maneuvering. The inner-loop pitch rate feedback is comprised of a proportional feedback gain, to improve damping of the short-period

American Institute of Aeronautics and Astronautics

mode. In the high speed regime, this feedback gain needs to be high to avoid any unstable short-period mode. The normal acceleration feedback, a proportional-integrator (PI) compensator, has not been implemented in our analysis since only roll-coupled maneuvers are considered.

2.   Lateral Control

Control of the lateral direction axis involves roll rate (p in rad/s) feedback to the aileron actuators. Roll rate feedback is used to improve roll damping and the roll-subsidence mode of the aircraft. Due to the inherent high roll damping associated with the F/A-18 aircraft at high speed, the roll rate feedback authority is usually reduced at high dynamic pressure. In the low speed regime, the roll rate feedback gain is increased to improve the Dutch roll damping. The roll rate feedback gain ranges between 0.8 at low speed to 0.08 at high speed. At 250 ft/s, flight condition described in this paper, a feedback gain of 0.8 is used to provide roll damping.

3.   Directional Control

Directional control involves feedback from yaw rate (r in rad/s) and lateral acceleration (a_y in g) to the rudder actuators. Yaw rate is fed back to the rudder to generate a yawing moment. Yaw rate feedback reduces yaw rate contribution to the Dutch-roll mode. In a steady state turn, there is always a constant nonzero yaw rate present. This requires the pilot to apply larger than normal rudder input to negate the effect of the yaw damper and make a coordinated turn. Hence, a washout filter is used to effectively eliminate this effect. The filter approximately differentiates the yaw rate feedback signal at low frequency, effectively eliminating yaw rate feedback at steady state conditions.[12] The lateral acceleration feedback contributes to reduce sideslip during turn coordination.
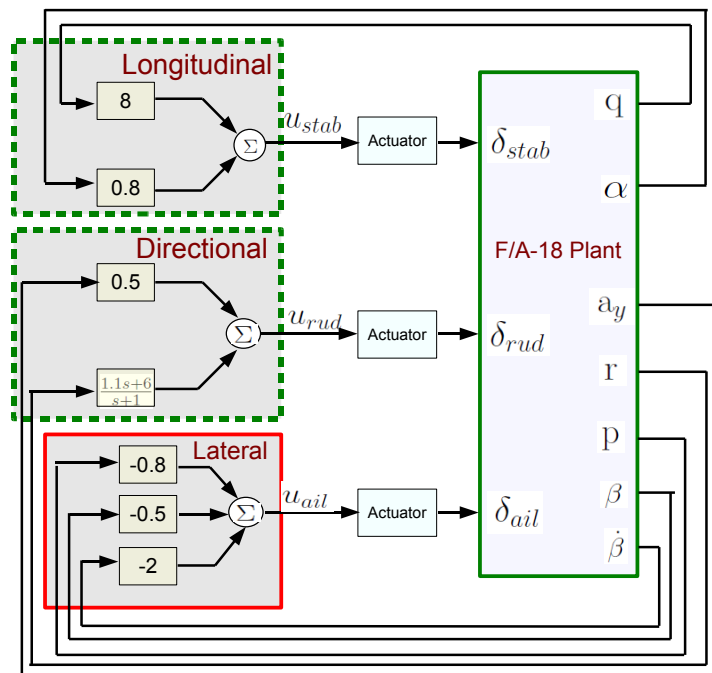
B.   Revised Control Law

Figure 5. F/A-18 Revised Flight Control Law

Figure 5 shows the architecture of the revised F/A-18 flight control law as described in the papers by Heller, David, & Holmberg[1] and Heller, Niewoehner, & Lawson.[19] The objective of the revised flight control law was to improve the departure resistance characteristics and full recoverability of the F/A-18 aircraft without sacrificing the maneuverability of the aircraft.[1] The significant change in the revised control law

American Institute of Aeronautics and Astronautics

was the additional sideslip (β in rad) and sideslip rate ($\dot{\beta}$ in rad/s) feedback to the aileron actuators. The sideslip feedback plays a key role in increasing the lateral stability in the $30 - 35°$ range of angle-of-attack. The sideslip rate feedback improves the lateral-directional damping. Hence, sideslip motion is damped even at high angles-of-attack. This feature is key to eliminating the falling leaf mode, which is an aggressive form of in-phase Dutch-roll motion. There are no direct measurements of sideslip and sideslip rate. Therefore, they are estimated for feedback. The sideslip and the sideslip rate feedback signals are computed based on already available signals from the sensors and using the kinematics of the aircraft. Proportional feedback has been implemented for these two feedback channels. The values of the proportional gains are $k_\beta = 0.5$ and $k_{\dot{\beta}} = 2$.

V.   Analysis

Linear robustness and nonlinear region-of-attraction analyses are performed to compare the baseline and the revised F/A-18 flight control laws. The linear analysis captures the local behavior of the system and is only valid around the equilibrium point of the linearization. Linear analysis does not provide insight into how the nonlinearities of the aircraft dynamics will affect the stability properties of the system. Two approaches are taken to analyze the effect of the nonlinearities. First, the closed-loop flight control systems are analyzed by using region-of-attraction estimation techniques to compute an inner estimate of the stability boundaries. Second, Monte Carlo simulations are performed on the closed-loop dynamics to estimate outer bounds of the stability boundaries. The linear robustness analysis has been performed using the *Robust Control Toolbox*.[20]

A.   Linear Analysis

The cubic polynomial model described in Appendix B is linearized around the flight condition of: $V_T = 250$ ft/s, altitude $=25,000$ ft at different bank angle turn, i.e, $\phi = 0^o$, 25°, 45°, 60°. Section III.E presents the operating points for the linear systems. The actuator states are excluded from both linear and nonlinear models. The actuators have very fast dynamics, as mentioned in Table 2, and their dynamics can be neglected without causing any significant variation in the analysis results. Validation and verification of flight control law relies heavily on applying linear analysis at trim points throughout the flight envelope. Linear analysis usually amounts to investigating robustness issues and possible worst-case scenarios around the operating points of interest.

1.   *Loopmargin Analysis*

Gain and phase margins provide stability margins for the closed-loop system. Poor gain and phase margins indicate poor robustness of the closed-loop system. A typical requirement for certification of a flight control law requires the closed-loop system to achieve at least $6dB$ of gain margin and 45^0 of phase margin. However, the classical loop-at-a-time SISO (Single-Input-Single-Output) margin can be unreliable for MIMO (Multi-Input-Multi-Output) systems. The F/A-18 aircraft closed- loop plants under consideration are multivariable; hence, we will perform both disk margin and multivariable margin analysis in addition to the classical loop-at-a-time margin analysis.

Classical Gain, Phase and Delay Margin Analysis: Classical gain, phase and delay margins provide robustness margins for each individual feedback channel with all the other loops closed. This loop-at-a-time margin analysis provides insight on the sensitivity of each channel individually. Table 4 provides the classical margins for both the baseline and the revised flight control laws. The results, presented in Table 4, are based on the unsteady ($\beta = 10^o$) bank turn maneuver at $\phi = 60^o$ (Plant 8). The baseline and revised flight control laws have very similar classical margins at the input channel. However, loop-at-a-time margin analysis can be unreliable for a multivariable system. Hence, multivariable loop margin analysis is necessary to understand how coupling between the channel effects the robustness properties.

Disk Margin Analysis: Disk margin analysis provides an estimate on how much combined gain/phase variations can be tolerated at each channel with other loops closed. The disk margin metric is very similar to an exclusion region on a Nichols chart. As with the classical margin calculation, coupling effects between channels may not be captured by this analysis. Table 5 provides the disk gain and phase variations at each

Table 4. Classical Gain & Phase Margin Analysis for Plant 8

Input Channel		Baseline	Revised
Aileron	Gain Margin	∞	27 dB
	Phase Margin	104°	93°
	Delay Margin	0.81 sec	0.44 sec
Rudder	Gain Margin	34 dB	34 dB
	Phase Margin	82°	76°
	Delay Margin	2.23 sec	1.99 sec
Stabilator	Gain Margin	∞	∞
	Phase Margin	91°	91°
	Delay Margin	0.24 sec	0.24 sec

loop for both the control laws. The results are based on the unsteady ($\beta = 10^o$) bank turn maneuver at $\phi = 60^o$ (Plant 8). The baseline flight control law achieves slightly better stability margins in the stabilator channel; while the revised flight control law has slightly better margins in the aileron channel. Overall, the disk margins between the two flight control laws are nearly indistinguishable. Disk margin analysis has not provided any definitive certificate on which of the two flight control law is more robust. The multivariable, simultaneous disk margin analysis across all channels may provide a better insight on which control law has better margins.

Table 5. Disk Margin Analysis for Plant 8

| Input Channel		Baseline	Revised
Aileron	Gain Margin	20 dB	∞
	Phase Margin	78°	90°
Rudder	Gain Margin	15 dB	14 dB
	Phase Margin	69°	67°
Stabilator	Gain Margin	∞	∞
	Phase Margin	90°	90°

Multivariable Disk Margin Analysis: The multivariable disk margin indicates how much simultaneous (across all channels), independent gain and phase variations can the closed-loop system tolerate before becoming unstable. This analysis is conservative since it allows independent variation of the input channels simultaneously. Figure 6 presents the multivaribale disk margin ellipses. Figure 6(a) is based on Plant 4 and Figure 6(b) is based on Plant 8. The mutivariable disk margin analysis certifies that for simultaneous gain & phase variations in each channel inside the region of the ellipses the closed-loop system remains stable. The mutivariable disk margin analysis for steady bank turn maneuvers, in Figure 6(a), shows both the baseline and the revised flight control laws have similar multivariable margins. For this steady maneuver, both the control laws can handle gain variation up to $\approx \pm 12.5$ dB and phase variation of $\approx \pm 64^o$ across channels. Figure 6(b) shows the mutivariable disk margin analysis for unsteady bank turn maneuvers. Here, the revised flight control law achieves slightly better margin (Gain margin $= \pm 11.3 dB$, Phase margin $= \pm 60^0$) than the baseline flight control law (Gain margin $= \pm 9.5 dB$, Phase margin $= \pm 54^0$). However, the differences in the margins between the two control laws is not significant enough to conclude which flight control law is susceptible to the falling leaf motion. Moreover, both the control laws achieve the typical margin requirement specification (6dB gain margin and 45^0 phase margin).

2. *Input Multiplicative Uncertainty*

Modeling physical systems perfectly is always a challenge. A mathematical model of the physical system always differs from the actual behavior of the system in many engineering problems. The F/A-18 aircraft
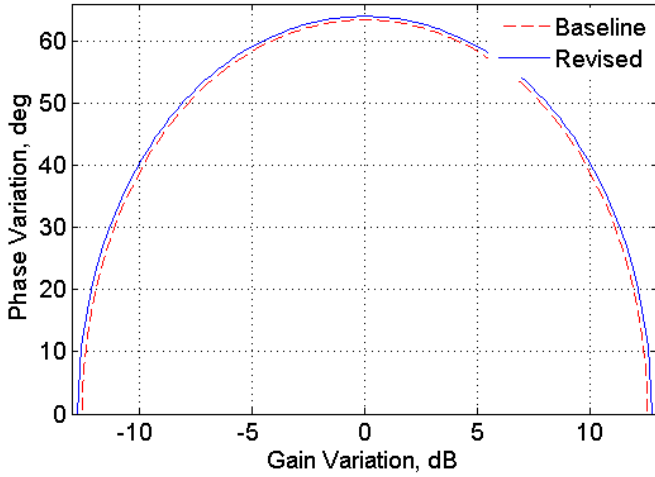
(a) Steady Maneuvers at $\phi = 60^o$
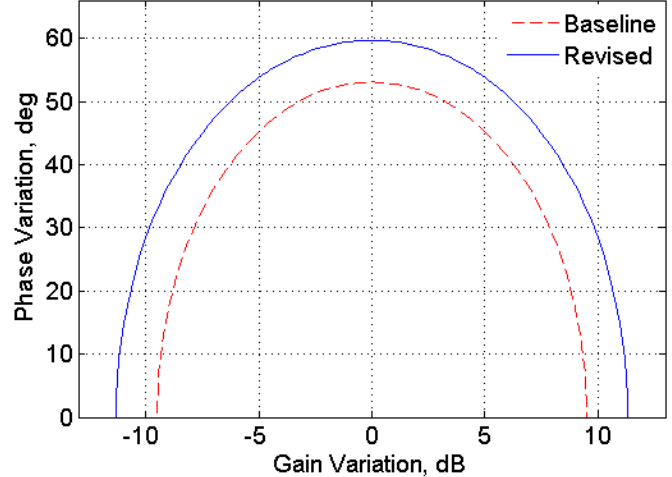
(b) Unsteady Maneuvers at $\phi = 60^o$

Figure 6. Disk Margin Analysis of the Baseline and Revised F/A-18 Flight Control Law
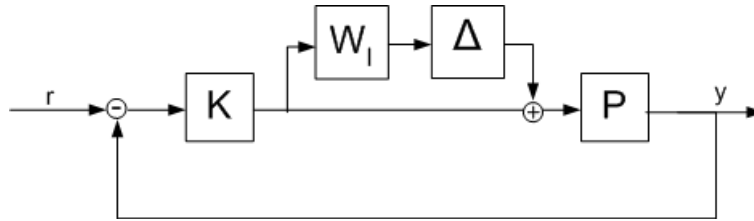

Figure 7. F/A-18 Input Multiplicative Uncertainty Structure

model presented in this paper is no exception. One approach is to account for the inaccuracies of the modeled aircraft dynamics as input multiplicative uncertainty.

Figure 7 shows the general uncertainty structure of the plant that will be considered in the input multiplicative uncertainty analysis. To assess the performance due to the inaccuracies of the modeled dynamics, we introduce multiplicative uncertainty, $W_I \Delta_{IM}$, in all four input channels. The uncertainty Δ_{IM} represents unit norm bounded unmodeled dynamics. The weighting function will be set to unity for analysis purpose, $W_I = I_{4\times4}$. We will perform the structured-singular-value (μ) analysis. The $\frac{1}{\mu}$ value measures the stability margin due to the uncertainty description in the system.

Diagonal Input Multiplicative Uncertainty: Figure 8 shows the μ plot of both the closed loops at both steady and unsteady bank maneuvers. The left subplot presents results based on plants 1-4, as mentioned in Table 3, for steady ($\beta = 0$) maneuvers, and the right subplot presents results based on plants 5-8 for unsteady ($\beta = 10^o$) maneuvers. Here the uncertainty, Δ_{IM}, has a diagonal structure. This models uncertainty in each actuation channel but no cross-coupling between the channels. The value of μ at each frequency ω is inversely related to the smallest uncertainty which causes the feedback system to have poles at $\pm j\omega$. Thus the largest value on the μ plot is equal to $1/k_m$ where k_m denotes the stability margin. In Figure 8(a), the peak value of μ is 0.97 ($k_m = 1.03$) for both the revised and baseline controller during steady maneuvers, which indicates a very robust flight control system. In addition, Figure 8(b) shows the peak value of μ for both the control laws at unsteady bank turn maneuvers. Here, the baseline flight controller exhibits a peak μ value of 1.25 ($k_m = 0.83$) and the revised flight controller achieves a μ value of 1.20 ($k_m = 0.80$). In both steady and unsteady maneuvers, both the controllers achieve similar stability margins for diagonal input multiplicative uncertainty across the input channel. These results corresponds well with the classical margin
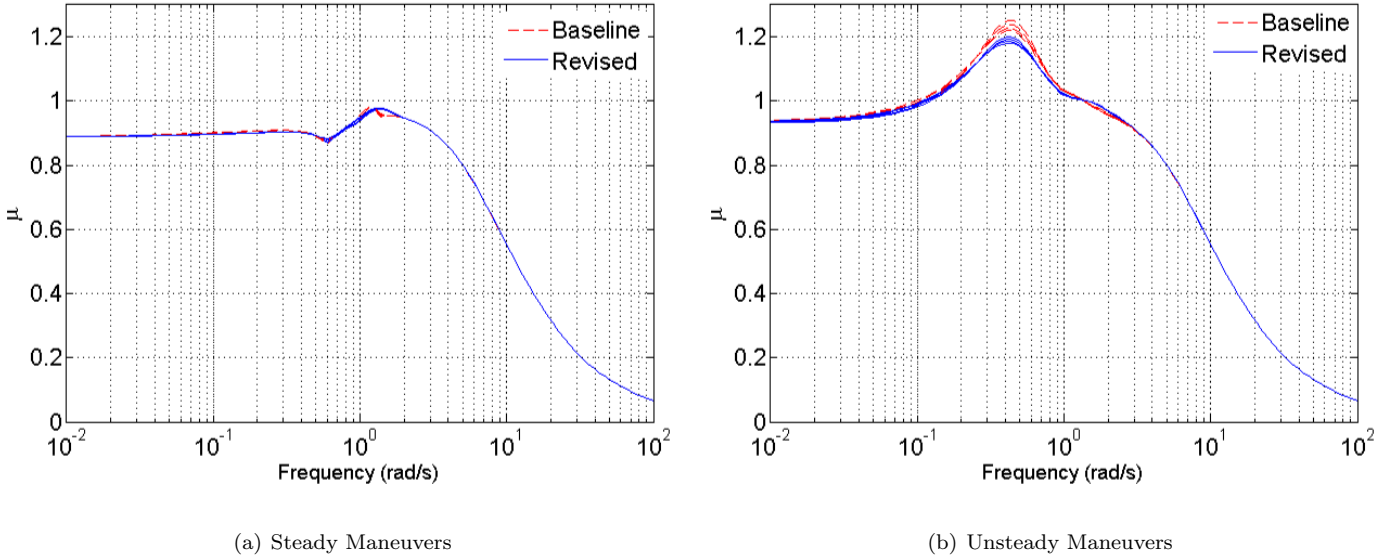
American Institute of Aeronautics and Astronautics

(a) Steady Maneuvers   (b) Unsteady Maneuvers

Figure 8. Diagonal Input Multiplicative Uncertainty Analysis of the Baseline and Revised F/A-18 Flight Control Law

results in Section V.A.1 .

Full Block Input Multiplicative Uncertainty: Figure 9 shows the μ plot for both steady and unsteady maneuvers. The left subplot presents results based on plants 1-4, as mentioned in Table 3, for steady ($\beta = 0$) maneuvers, and the right subplot presents results based on plants 5-8 for unsteady ($\beta = 10^o$) maneuvers. In this analysis, Δ_{IM} is allowed to be a full block uncertainty. This uncertainty structure models the effects of dynamic cross-coupling between the channels to determine how well the flight control laws are able to handle the coupling at the input to the F/A-18 actuators. As mentioned before, the falling leaf motion is an exaggerated form of in-phase Dutch-roll motion with large coupling in the roll-yaw direction. Increased robustness of the flight control law with respect to the full Δ_{IM} is associated with its ability to mitigate the onset of the falling leaf motion. Figure 9(a) shows the μ analysis for steady maneuvers. In this case, both the baseline and revised flight control law achieves similar stability margin ($\mu = 1.02$ and $k_m = 0.98$). Figure 9(b) shows the μ analysis for unsteady maneuvers. Here, the baseline flight controller exhibits a peak μ value of 1.25 ($k_m = 0.83$) and the revised flight controller achieves a μ value of 1.20 ($k_m = 0.80$). In both steady and unsteady maneuvers, both the controllers achieve similar stability margins for full input multiplicative uncertainty across the input channels.

Robustness analysis with respect to input multiplicative uncertainty (both full block and diagonal) across input channels has not detected any performance issue with the baseline flight control law compare to the revised flight control law. At this point, the linear analysis shows both controllers are very robust with similar stability margins and that should mitigate the onset of the falling leaf motion.

3. Robustness Analysis to Parametric Uncertainty

So far we have provided a stability analysis with respect to unstructured dynamic uncertainty at the model inputs. Robustness analysis of flight control system with structured uncertainty is another important analysis in validating closed-loop robustness and performance.[21] Moreover, robustness assessment of the flight control law due to the nonlinear variations of aerodynamic coefficients over the flight envelope needs to be considered. Including parametric uncertainty models into the analysis is one approach to address this issue. Both controllers are examined with respect to robustness in the presence of parametric variations in the plant model. To this end, we represented the stability derivatives of the linearized model with $\pm 10\%$ uncertainty around their nominal values. These terms are chosen carefully to represent the stability characteristics of
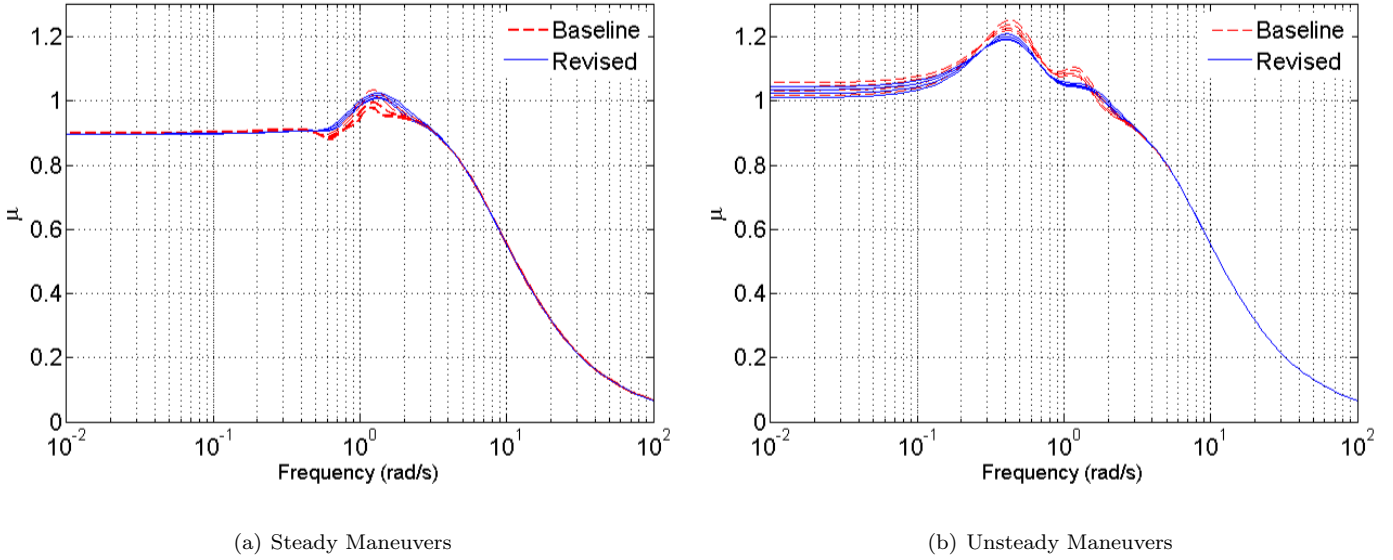
(a) Steady Maneuvers   (b) Unsteady Maneuvers

Figure 9. Full Block Input Multiplicative Uncertainty Analysis of the Baseline and Revised F/A-18 Flight Control Law

the F/A-18 aircraft that play an important role in the falling leaf motion. These terms are related to the entries of the linearized open-loop A matrix. The terms in the lateral directions are: sideforce due to sideslip (Y_β); rolling moment due to sideslip (L_β); yawing moment due to sideslip (N_β); roll damping (L_p); yaw damping (N_r). The following longitudinal terms have also been considered: pitch damping (M_q); normal force due to pitch rate (Z_q); pitch stiffness (M_α). Cook[10] provides a detailed description of these terms. The lateral aerodynamic terms: Y_β, L_β, N_β, L_p, and N_r correspond respectively to the $(1,1)$, $(2,1)$, $(3,1)$, $(2,2)$, and $(3,3)$ entries of the linearized A matrix presented in previous section. The longitudinal aerodynamic terms: M_q, Z_q, and M_α correspond respectively to the $(6,6)$, $(5,6)$, and $(6,5)$ entries of the same linearized A matrix.

Figure 10 shows the μ plot (for both steady and unsteady maneuvers) of both closed-loop systems with respect to this parametric uncertainty. Again, the left subplot presents results based on plants 1-4, as mentioned in Table 3, for steady ($\beta = 0^o$) maneuvers, and the right subplot presents results based on plants 5-8 for unsteady ($\beta = 10^o$) maneuvers. For steady maneuvers, in Figure 10(a), the stability margin for parametric uncertainty in the aerodynamic coefficients of the revised controller ($\mu = 0.092$ and $k_m = 10.8$) is approximately 1.3 times larger than that of the baseline controller ($\mu = 0.115$ and $k_m = 8.7$). For unsteady maneuvers, in Figure 10(b), the stability margin for parametric uncertainty in the aerodynamic coefficients of the revised controller ($\mu = 0.109$ and $k_m = 9.17$) is approximately 1.2 times larger than that of the baseline controller ($\mu = 0.131$ and $k_m = 7.63$). Hence, the revised flight controller is more robust to error in aerodynamic derivatives than the baseline design, but overall both flight controllers are very robust designs.

To this point, the linear robustness analysis indicate both the revised and baseline flight control laws are slightly less robust for unsteady maneuvers compared to the steady maneuvers. However, both the control laws achieve similar robustness properties separately for steady and unsteady maneuvers. The linear robustness analysis for the F/A-18 flight control laws do not indicate any dramatic improvement in departure resistance for the revised flight control compare to the baseline flight control law. This is contrary to the fact that the revised flight control law has been tested to be more robust as it is able to suppress the falling leaf motion problem in the F/A-18 Hornet aircraft. Hence, this motivates us to investigate the nonlinear stability analysis for both the flight control laws.
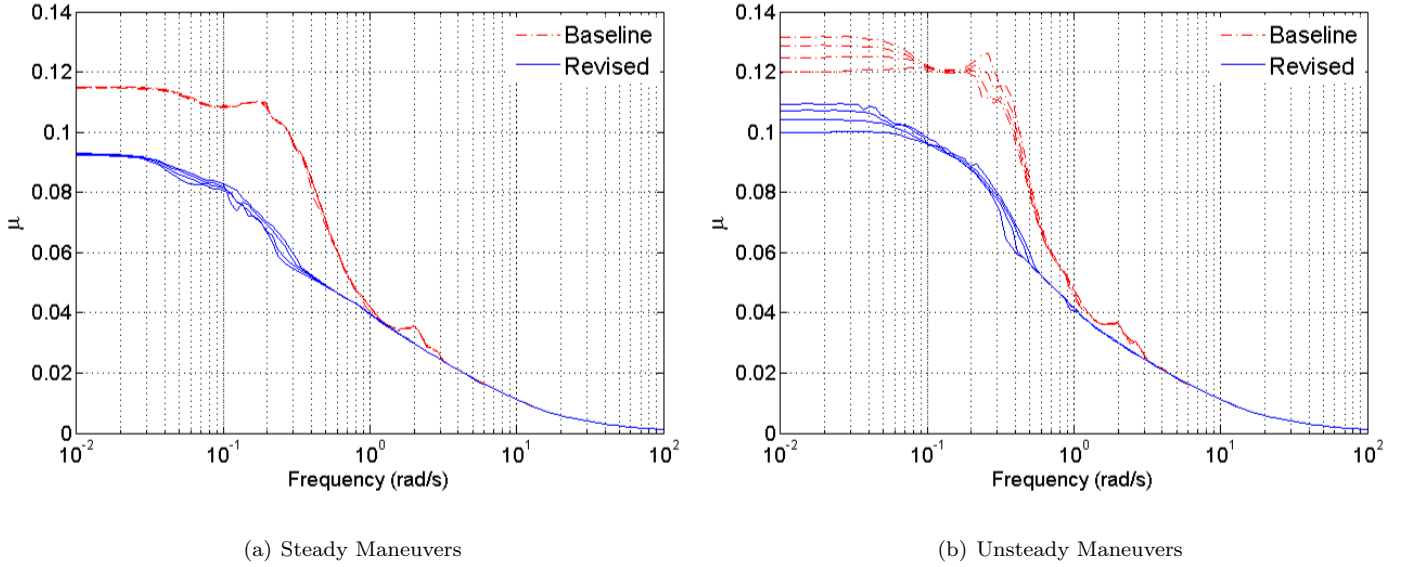
American Institute of Aeronautics and Astronautics

(a) Steady Maneuvers   (b) Unsteady Maneuvers

Figure 10. Stability Analysis of the Baseline and Revised F/A-18 Flight Control Law with Real Parametric Uncertainty in Aerodynamic Coefficients

B. Nonlinear Analysis

The falling leaf motion is due to nonlinearities in the aircraft dynamics and cannot be replicated in simulation by linear models. Thus the linear analyses, which are local analyses only valid near an operating point, may be insufficient for analyzing the falling leaf motion. We propose to use nonlinear region-of-attraction analysis to study the F/A-18 dynamics. This analysis is based on a fundamental difference between asymptotic stability for linear and nonlinear systems. For linear systems asymptotic stability of an equilibrium point is a global property. In other words, if the equilibrium point is asymptotically stable then the state trajectory will converge back to the equilibrium when starting from any initial condition. A key difference with nonlinear systems is that equilibrium points may only be locally asymptotically stable. Khalil[22] and Vidyasagar[23] provide good introductory discussions of this issue. The region-of-attraction (ROA) of an asymptotically stable equilibrium point is the set of initial conditions whose state trajectories converge back to the equilibrium.[22] If the ROA is small, then a disturbance can easily drive the system out of the ROA and the system will then fail to come back to the stable equilibrium point. Thus the size of the ROA is a measure of the stability properties of a nonlinear system around an equilibrium point. This provides the motivation to estimate the region-of-attraction (ROA) for an equilibrium point of a nonlinear system. In this section we describe our technical approach to estimating the ROA and its application to estimate the ROA for the closed loop F/A-18 system with both the baseline and revised control laws. Results presented in this section are based on the models described in Appendix E. Moreover, the actuators' rate and position limit, presented in Table 2, are not considered in the analysis.

1. Technical Approach

We consider autonomous nonlinear dynamical systems of the form:

$$\dot{x} = f(x), \; x(0) = x_0 \tag{1}$$

where $x \in \mathbb{R}^n$ is the state vector. We assume that $x = 0$ is a locally asymptotically stable equilibrium point. Formally, the ROA is defined as:

$$R_0 = \left\{ x_0 \in \mathbb{R}^n : \text{ If } x(0) = x_0 \text{ then } \lim_{t \to \infty} x(t) = 0 \right\} \tag{2}$$

American Institute of Aeronautics and Astronautics

Computing the exact ROA for nonlinear dynamical systems is very difficult. There has been significant research devoted to estimating invariant subsets of the ROA.[5, 24–31] Our approach is to restrict the search to ellipsoidal approximations of the ROA. The ellipsoid is specified by $\{x_0^T N x_0 \leq \beta\}$ where $N = N^T > 0$ is a user-specified matrix which determines the shape of the ellipsoid. Given N, the problem is to find the largest ellipsoid contained in the ROA:

$$\beta^* = \max \beta \tag{3}$$
$$\text{subject to: } \{x_0^T N x_0 \leq \beta\} \subset R_0$$

Determining the best ellipsoidal approximation to the ROA is still a challenging computational problem. Instead we will attempt to solve for upper and lower bounds satisfying $\underline{\beta} \leq \beta^* \leq \bar{\beta}$. If these upper and lower bounds are close then we have approximately solved the best ellipsoidal approximation problem given in Equation 3.

The upper bounds are computed via a search for initial conditions leading to divergent trajectories. If $\lim_{t\to\infty} x(t) = +\infty$ when starting from $x(0) = x_{0,div}$ then $x_{0,div} \notin R_0$. If we define $\bar{\beta}_{div} := x_{0,div}^T N x_{0,div}$ then $\{x_0^T N x_0 \leq \bar{\beta}_{div}\} \not\subset R_0$. Thus $\bar{\beta}_{div}$ is a true upper bound on β^* and $\{x_0^T N x_0 \leq \bar{\beta}_{div}\}$ is an outer approximation of the best ellipsoidal approximation to the ROA. We use an exhaustive Monte Carlo search to find the tightest possible upper bound on β^*. Specifically, we randomly choose initial conditions starting on the boundary of a large ellipsoid: Choose x_0 satisfying $x_0^T N x_0 = \beta_{try}$ where β_{try} is sufficiently large that $\beta_{try} \gg \beta^*$. If a divergent trajectory is found, then the initial condition is stored and an upper bound on β^* is computed. β_{try} is then decreased by a factor of 0.995 and the search continues until a maximum number of simulations is reached. $\bar{\beta}_{MC}$ will denote the smallest upper bound computed with this Monte Carlo search.

The lower bounds are computed using Lyapunov functions and recent results connecting sums-of-squares polynomials to semidefinite programming. To compute these bounds we need to further assume that the vector field $f(x)$ in the system dynamics (Equation 1) is a polynomial function. We briefly describe the computational algorithm here and full algorithmic details are provided elsewhere.[2–4, 32–35] Lemma 1 is the main Lyapunov theorem used to compute lower bounds on β^*. This specific lemma is proved by Tan[4] but very similar results are given in textbooks, e.g. by Vidyasagar.[23]

Lemma 1 *If there exists a continuously differentiable function $V : \mathbb{R}^n \to \mathbb{R}$ such that:*

- $V(0) = 0$ *and* $V(x) > 0$ *for all* $x \neq 0$

- $\Omega_\gamma := \{x \in \mathbb{R}^n \ : \ V(x) \leq \gamma\}$ *is bounded.*

- $\Omega_\gamma \subset \{x \in \mathbb{R}^n \ : \ \nabla V(x) f(x) < 0\}$

then for all $x \in \Omega_\gamma$, the solution of Equation 1 exists, satisfies $x(t) \in \Omega_\gamma$ for all $t \geq 0$, and $\Omega_\gamma \subset R_0$.

A function V satisfying the conditions in Lemma 1 is a Lyapunov function and Ω_γ provides an estimate of the region of attraction. Any subset of Ω_γ is also inside the ROA. In principle we can compute a lower bound on β^* by solving the maximization:

$$\underline{\beta} := \max \beta \tag{4}$$
$$\text{subject to: } \{x_0^T N x_0 \leq \beta\} \subset \Omega_\gamma$$

Our computational algorithm replaces the set containment constraint with a sufficient condition involving non-negative functions:

$$\underline{\beta} := \max \beta \tag{5}$$
$$\text{subject to: } s(x) \geq 0 \ \forall x$$
$$- (\beta - x^T N x) s(x) + (\gamma - V(x)) \geq 0 \ \forall x$$

The function $s(x)$ is a decision variable of the optimization, i.e. it will be found as part of the optimization. It is a "multiplier" function. It is straight-forward to show that the two non-negativity conditions in Optimization 5 are a sufficient condition for the set containment condition in Optimization 4. If both $V(x)$ and $s(x)$ are restricted to be polynomials then both constraints involve the non-negativity of polynomial functions. A sufficient condition for a generic multi-variate polynomial $p(x)$ to be non-negative is the existence

American Institute of Aeronautics and Astronautics

of polynomials $\{g_1, \ldots, g_n\}$ such that $p = g_1^2 + \cdots + g_n^2$. A polynomial which can be decomposed in this way is rather appropriately called a sum-of-squares (SOS). Finally, if we replace the non-negativity conditions in Optimization 5 with SOS constraints, then we arrive at an SOS optimization problem:

$$\underline{\beta} := \max \beta \tag{6}$$
$$\text{subject to: } s(x) \text{ is } SOS$$
$$- (\beta - x^T N x) s(x) + (\gamma - V(x)) \text{ is } SOS$$

There are connections between SOS polynomials and semidefinite matrices. Moreover, optimization problems involving SOS constraints can be converted and solved as a semidefinite programming optimization. Importantly, there is freely available software to set up and solve these problems.[6,36,37]

The choice of the Lyapunov function which satisfies the conditions of Lemma 1 has a significant impact on the quality of the lower bound, $\underline{\beta}$. The simplest method is to compute $P > 0$ that solves the Lyapunov equation $A^T P + PA = -I$. $A := \frac{\partial f}{\partial x}\big|_{x=0}$ is the linearization of the dynamics about the origin. $V_{LIN}(x) := x^T P x$ is a quadratic Lyapunov function since $x = 0$ is assumed to be a locally asymptotically stable equilibrium point. Thus we can solve for the largest value of γ satisfying the set containment condition in Lemma 1: $\Omega_\gamma \subset \{x \in \mathbb{R}^n : \nabla V_{LIN}(x)f(x) < 0\}$. This problem can also be turned into an SOS optimization with "multiplier" functions as decision variables. $\underline{\beta}_{LIN}$ will denote the lower bound obtained using the quadratic Lyapunov function obtained from linearized analysis.

Unfortunately, $\underline{\beta}_{LIN}$ is typically orders of magnitude smaller than the upper bound $\bar{\beta}_{MC}$. Several methods to compute better Lyapunov functions exist, including V-s iterations,[32–35] bilinear optimization,[4] and use of simulation data.[2,3] We applied the V-s iteration starting from V_{LIN}. In the first step of the iteration, the multiplier functions and $\underline{\beta}_{LIN}$ are computed. Then the multiplier functions are held fixed and the Lyapunov function candidate becomes the decision variable. The SOS constraints of this new problem are those which arise from the two set containment conditions: $\Omega_\gamma \subset \{x \in \mathbb{R}^n : \nabla V_{LIN}(x)f(x) < 0\}$ and $\{x_0^T N x_0 \leq \beta\} \subset \Omega_\gamma$. In the next iteration, the multiplier functions are again decision variables and a lower bound is computed using the new Lyapunov function computed in the previous iteration. The V-s iteration continues as long as the lower bound continues to increase. In this iteration, we can allow Lyapunov functions of higher polynomial degree. Increasing the degree of the Lyapunov function will improve the lower bound at the expense of computational complexity. The computational time grows very rapidly with the degree of the Lyapunov function and so degree 4 candidates are about the maximum which can be used for problems like the F/A-18 analysis. $\underline{\beta}_2$ and $\underline{\beta}_4$ denote the best lower bounds computed with the V-s iteration for quadratic and quartic Lyapunov functions.

2. ROA Analysis for F/A-18

ROA lower bounds $\underline{\beta}$ for the F/A-18 using with the V-s iteration are computed in this section . The analysis will be performed for the F/A-18 aircraft operating at a steady ($\beta = 0$) bank turn of $\phi = 60^o$. This ROA analysis uses the cubic polynomial models for 60° steady bank turn maneuver (Appendix E). The ordering of the state vector is $x^T := [\beta, \text{ p}, \text{ r}, \phi, \alpha, \text{ q}, x_c]$. The shape matrix for the ellipsoid is chosen to be $N := (5)^2 \cdot diag(5^o, 20^o/s, 5^o/s, 45^o, 25^o, 25^o/s, 25^o)^{-2}$. This roughly scales each state by the maximum magnitude observed during flight conditions. The factor of $(5)^2$ normalizes the largest entry of the matrix N to be equal to one. The ellipsoid, $x^T N x = \underline{\beta}$, defines the set of initial conditions for which the control law will bring the aircraft back to its trim point. If the aircraft is perturbed due to a wind gust or other upset condition but remains in the ellipsoid then the control law will recover the aircraft and bring it back to trim. In other words the ellipsoid defines a safe flight envelope for the F/A-18. Hence, the ROA provides a measure of how much perturbation the aircraft can tolerate before it becomes unstable. The value of the $\underline{\beta}$ can be thought of as 'nonlinear stability margin', similar to the linear stability margin (k_m) concept presented in Section V.A . However, these two margins are not comparable to each other.

As previously mentioned, increasing the degree of the Lyapunov function will improve the lower bound estimate of the ROA. We first computed a bound using the quadratic Lyapunov function from linearized analysis. This method has been proposed for validation of flight control laws.[21] We computed $\underline{\beta}_{LIN} = 8.05 \times 10^{-5}$ for the baseline control law and $\underline{\beta}_{LIN} = 1.91 \times 10^{-4}$ for the revised control. Unfortunately these lower bounds are not particularly useful since they are two to three orders of magnitude smaller than
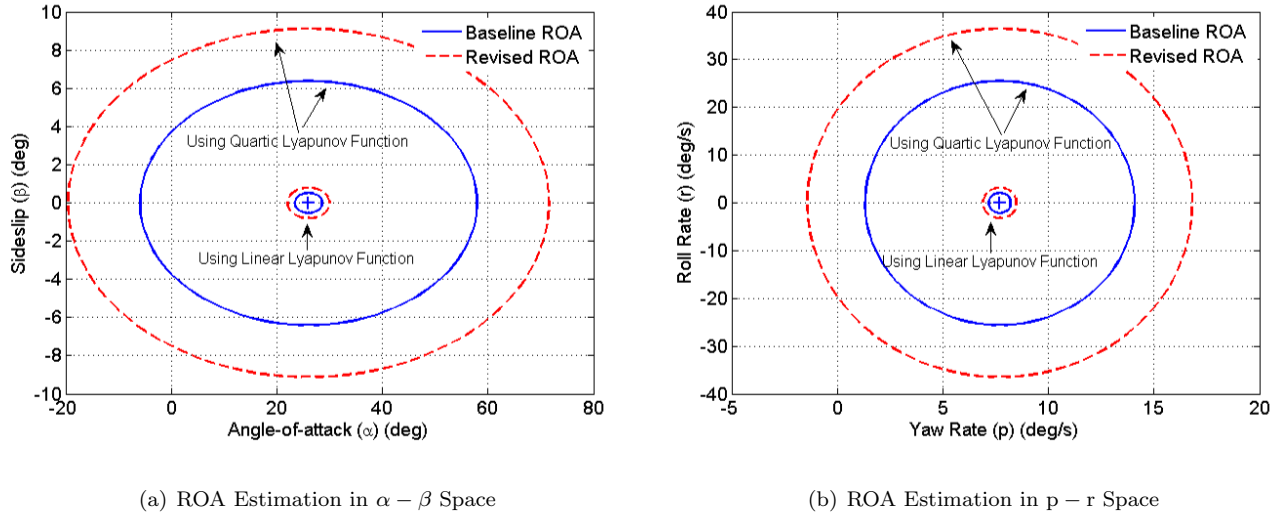
American Institute of Aeronautics and Astronautics

(a) ROA Estimation in $\alpha - \beta$ Space

(b) ROA Estimation in p − r Space

Figure 11. Estimated Lower Bound of ROA with both Linearized and Quartic Lyapunov Function

the corresponding upper bounds computed via Monte Carlo search (see Section V.B.3). Next, lower bounds with the V-s iteration using quadratic and quartic Lyapunov functions are computed. The V-s iteration with quadratic Lyapunov functions gives $\underline{\beta}_2 = 3.45 \times 10^{-3}$ for the baseline control law and $\underline{\beta}_2 = 9.43 \times 10^{-3}$ for the revised control law. The V-s iteration with quartic Lyapunov functions is $\underline{\beta}_4 = 1.24 \times 10^{-2}$ for the baseline control law and $\underline{\beta}_4 = 2.53 \times 10^{-2}$ for the revised control law. These bounds are significantly larger than the bounds obtained for the linearized Lyapunov function. A sixth order Lyapunov function would lead to improved lower bounds but with a significant increase in computation time.

The lower (inner) bounds on the region-of-attraction can be visualized by plotting slices of the ellipsoid $p(x) = \underline{\beta}$. Figure 11 shows slices of the ellipsoid in the α-β (left subplot) and p-r (right subplot) planes. The results for the linearized Lyapunov function and quartic Lyapunov function are shown in each plot. As mentioned previously, the use of the Lyapunov function from linear analysis has been proposed for validating flight control laws.[21] The slices in Figure 11 show that this method is much more conservative than the results obtained using the quartic Lyapunov function.

The slices for the quartic Lyapunov functions demonstrate that the ROA estimate for the revised control law is larger than for the baseline control law. For example, from the α-β slice we conclude the baseline controller will return to the trim condition for initial perturbations in an ellipse defined by β between -6.4^o and $+6.4^o$ and α between -5.9^o and $+57.9^o$. The revised controller will return to the trim condition for initial perturbations in an ellipse defined by β between -9.1^o and $+9.1^o$ and α between -19.6^o and $+71.6^o$. In fact, the robustness improvement for the revised controller is more dramatic if we consider the volume of the ROA estimate. The volume of the ellipsoid $p(x) = \underline{\beta}$ is proportional to $\beta^{(n/2)}$ where n is the state dimension. Thus the ROA estimate obtained by the revised control law has a volume which is $(\underline{\beta}_{4,rev}/\underline{\beta}_{4,base})^{3.5}$ greater than that obtained by the linearized Lyapunov function. This corresponds to a volume increase of 12.1 for the quartic Lyapunov functions.

This is the first application of the nonlinear region of attraction analysis techniques to an actual flight control problem. However, this nonlinear analysis imposes a limitation that the dynamics of the aircraft need to be described by the polynomial functions of the states. Hence, the caveat with this nonlinear analysis results is that the size of the ROA may be larger than where the polynomial model is valid. In this paper, the aerodynamic coefficients have been fitted over a gridded α - β space of $-20° \leq \beta \leq 20°$, and $-10° \leq \alpha \leq 40°$. However, the results shown in Figure 11 go outside the bounds of this gridding. Hence, the results may not be valid over the entire region shown in the figure.

American Institute of Aeronautics and Astronautics

3. Monte Carlo Analysis for F/A-18

In the previous section we computed lower bounds on the best ellipsoidal ROA approximation. In this section we provide upper bounds computed via a Monte Carlo search for unstable trajectories. Closeness of the upper/lower bounds means that we have approximately solved the best ellipsoidal ROA approximation problem.

The Monte Carlo search was described in Section V.B.1 . We performed the search with a maximum of 2 million simulations each for the baseline and revised control laws. The baseline control law provides an upper bound of $\bar{\beta}_{MC} = 1.56 \times 10^{-2}$ whereas the revised control law provides an upper bound of $\bar{\beta}_{MC} = 2.95 \times 10^{-2}$. The search also returns an initial condition x_0 on the boundary of the ellipsoid, i.e. $p(x_0) = x_0^T N x_0 = \bar{\beta}_{MC}$, that causes the system to go unstable. Hence, the value of the $\bar{\beta}_{MC}$ provides an upper bound of the ROA for the F/A-18 aircraft. This is complementary information to that provided by the Lyapunov-based lower bounds. The Monte Carlo search returned the following initial condition for the closed system with the baseline control law:

$$x_0 = [-1.1206^o, \ -12.3353^o/s, \ 1.5461^o/s, \ -5.8150^o, \ 28.9786^o, \ 9.9211^o/s, \ 0]^T$$

This initial condition satisfies $p(x_0) = 1.56 \times 10^{-2}$. The left subplot of Figure 12(a) shows the unstable response of the baseline system resulting from this initial condition. Decreasing the initial condition slightly leads to a stable response. The right subplot of Figure 12(a) shows the stable system response when starting from $0.995x_0$. For the revised control law the Monte Carlo search returned the following initial condition:

$$x_0 = [0.3276^o, \ -8.0852^o/s, \ 2.8876^o/s, \ -2.1386^o, \ 44.8282^o, \ 9.9829^o/s, \ 0]^T$$

This initial condition satisfies $p(x_0) = 2.95 \times 10^{-2}$ and the left subplot of Figure 13(a) shows the unstable response of the revised system resulting from this initial condition. Decreasing the initial condition slightly leads to a stable response. The right subplot of Figure 13(a) shows the stable system response when starting from $0.995x_0$.

However, the actuator exceeds the physical limit in all cases presented above. In the analysis presented in this paper, we have ignored the saturation and rate limits of the actuator. This issue needs to be addressed in the future.

(a) Unstable Trajectory with IC s.t. $x_0^T N x_0 = 0.0155$
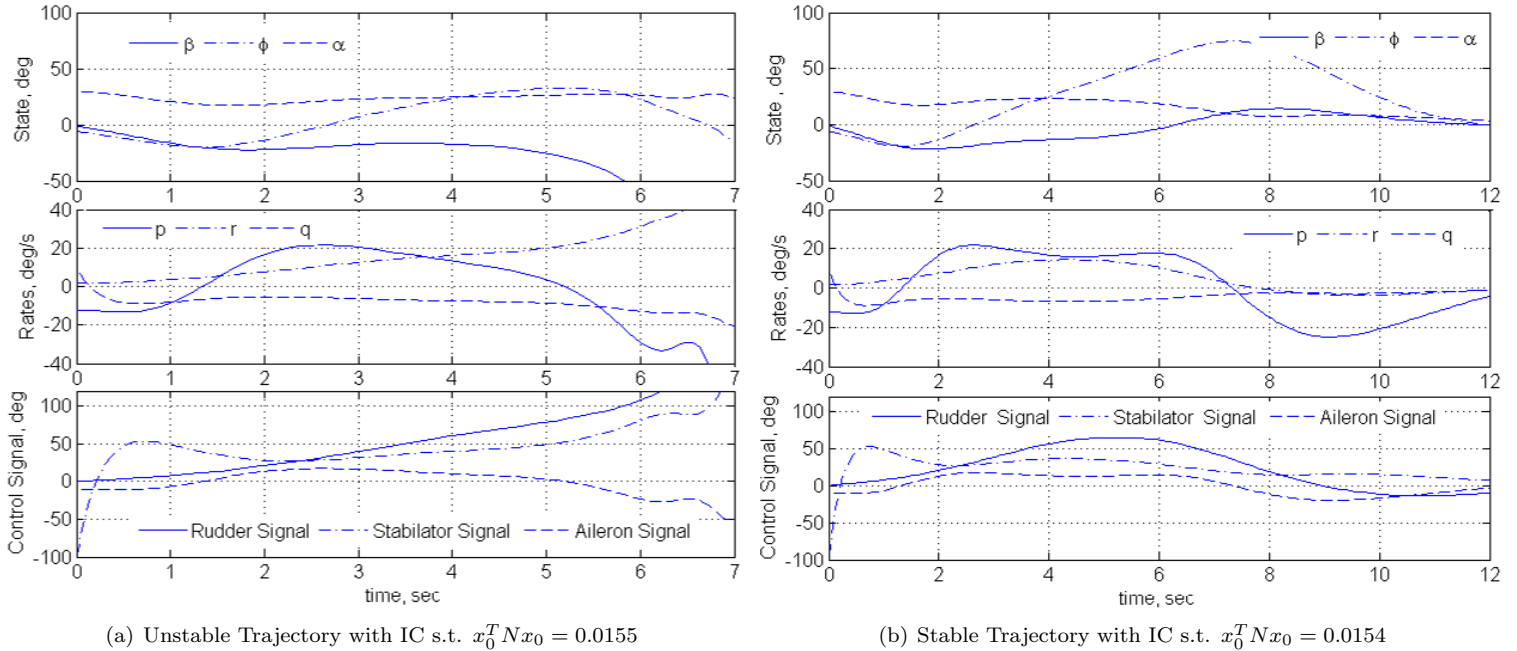(b) Stable Trajectory with IC s.t. $x_0^T N x_0 = 0.0154$

Figure 12. Time Response of F/A-18 Aircraft Baseline Closed Loop Model

At this point, we have computed the lower and upper bounds on β^*. Figure 14 shows slices of the inner/outer approximations of the best ellipsoidal ROA approximation for both the baseline and revised

American Institute of Aeronautics and Astronautics

(a) Unstable Trajectory with IC s.t. $x_0^T N x_0 = 0.0295$ (b) Stable Trajectory with IC s.t. $x_0^T N x_0 = 0.0294$
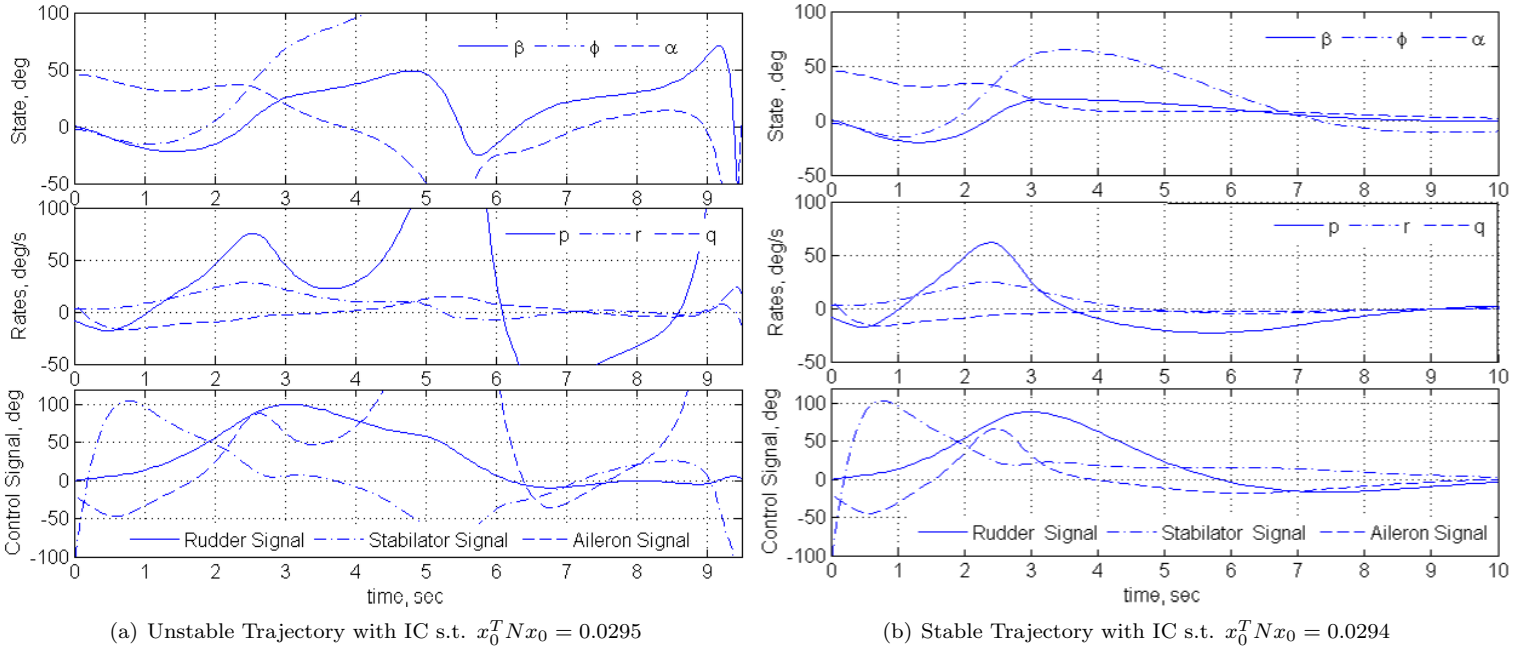
Figure 13. Time Response of F/A-18 Aircraft Revised Closed Loop Model

control laws. The blue solid lines show the slices of the inner bounds obtained from quartic Lyapunov analysis. Every initial condition within the blue ellipses will return to the trim condition (marked as a '+'). The red dashed lines show the slices of the outer bounds obtained from Monte Carlo analysis. There is at least one initial condition on the outer ellipsoid which leads to a divergent trajectory. The initial condition leading to a divergent trajectory does not necessarily lie on the slice of the ellipsoid shown in the figure. The closeness of the inner and outer ellipsoids means that we have solved, for engineering purposes, the best ROA ellipsoid problem.

Again, the aerodynamic coefficients have been fitted over a gridded α - β space of $-20° \leq \beta \leq 20°$, and $-10° \leq \alpha \leq 40°$. Hence, the results shown in Figure 14 may not be valid over the entire region as shown in the figure itself.
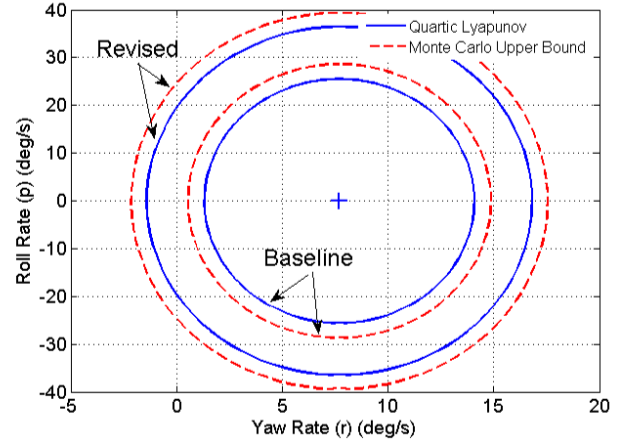
C. Summary

Table 6 summarizes the stability analysis results described in this section. There are several key points to be gathered from this analysis. First, the F/A-18 aircraft with the baseline control law was susceptible to the falling leaf motion. However, the linear robustness analysis did not detect any stability issues with this control law. Second, the revised control law demonstrated an ability to suppress the falling leaf motion in the F/A-18 aircraft in flight tests. However, the linear analyses did not show a significant improvement in the stability and robustness properties of the revised control law as compared to the baseline control law. Hence, based on the linear analyses alone both controllers should have mitigated the effect of the falling leaf motion. In contrast, the nonlinear analysis showed that the revised control law leads to a significant increase in the ROA estimate over the baseline design. This implies that the closed-loop system with the revised control law is more robust to disturbances and upset conditions. It is important to note that the region of attraction analysis accounts for significantly nonlinearities in the aircraft dynamics. This makes the analysis more applicable to highly nonlinear flight phenomenon such as the falling leaf mode.

VI.   Conclusion

In this paper, we have compared the stability and robustness properties of the two control laws (the baseline and the revised) of the F/A-18 aircraft using linear robustness concepts and nonlinear region-

American Institute of Aeronautics and Astronautics
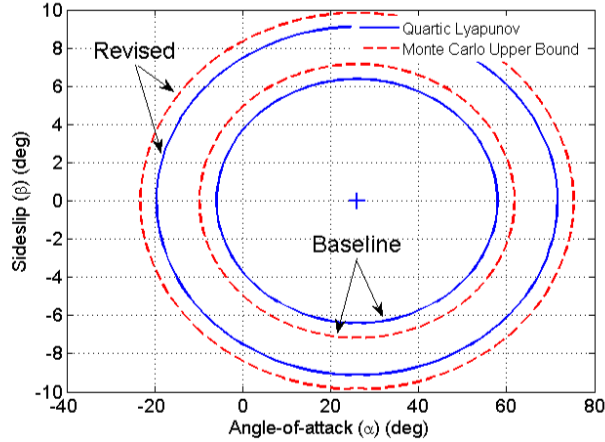
(a) Estimation of α-β Region-of-Attraction

(b) Estimation of p -r Region-of-Attraction

Figure 14. Lower and Upper Bound Estimate of ROA for Baseline and Revised Flight Control Law around Steady 60° Bank Turn

Table 6. Summary of Analysis Results

Linear Analysis	Baseline	Revised
Multivariable Loop Phase Margin	$\pm 63.4°$	$\pm 64.0°$
Multivariable Loop Gain Margin (dB)	± 12.53	± 12.73
Diagonal Input Multiplicative: $(k_m = \frac{1}{\mu})$	1.03	1.03
Full Input Multiplicative: $(k_m = \frac{1}{\mu})$	0.98	0.98
Parametric Uncertainty: $(k_m = \frac{1}{\mu})$	8.70	10.8
Nonlinear Analysis: $\{x^{\mathrm{T}}Nx \le \beta^*\}$		
Linearized Lyapunov Function,$\underline{\beta}_{lin}$	8.05×10^{-5}	1.91×10^{-4}
Generic Quadratic Lyapunov Function, $\underline{\beta}_2$	3.45×10^{-3}	9.43×10^{-3}
Generic Quartic Lyapunov Function, $\underline{\beta}_4$	1.24×10^{-2}	2.53×10^{-2}
Monte Carlo Simulation, $\bar{\beta}_{MC}$	1.56×10^{-2}	2.95×10^{-2}

of-attraction analysis tools. The nonlinear ROA analysis showed that the revised control law has better robustness properties compared to the baseline control law, whereas the linear analysis showed similar stability margins for both the control laws. Sum-of-Squares programming has been used to establish guaranteed stability regions for the nonlinear F/A-18 aircraft models. This is the first time that this technique has been successfully applied to a real physical system. This approach provides a guaranteed stability certificate for the control law as opposed to the widely used exhaustive Monte Carlo simulation technique.

Acknowledgments

Appendix

A. Full Model

The full six degree-of-freedom F/A-18 Hornet aircraft model is presented in this section. This model is not directly used for analysis presented in this paper, but is included for completeness.

1. Equations of Motion

The equations of motion described are taken from the report (chapter 4) by Napolitano and Spagnuolo.[11] The state variables are:

$$\mathbf{X}^{\mathrm{T}} = [V_T \quad \alpha \quad \beta \quad p \quad q \quad r \quad \phi \quad \theta \quad \psi]$$

The following three equations describe the force equations of the aircraft:

$$
\dot{V}_T = -\frac{\bar{q}S_{ref}}{m}(C_D \cos\beta - C_Y \sin\beta) + g(\cos\phi\cos\theta\sin\alpha\cos\beta + \sin\phi\cos\theta\sin\beta
$$
$$
- \sin\theta\cos\alpha\cos\beta) + \frac{T}{m}\cos\alpha\cos\beta
$$
$$
\dot{\alpha} = -\frac{\bar{q}S_{ref}}{mV_T\cos\beta}C_L + q - \tan\beta(p\cos\alpha + r\sin\alpha)
$$
$$
+ \frac{g}{V_T\cos\beta}(\cos\phi\cos\theta\cos\alpha + \sin\alpha\sin\theta) - \frac{T\sin\alpha}{mV_T\cos\beta}
$$
$$
\dot{\beta} = \frac{\bar{q}S_{ref}}{mV_T}(C_Y\cos\beta + C_D\sin\beta) + p\sin\alpha - r\cos\alpha + \frac{g}{V_T}\cos\beta\sin\phi\cos\theta
$$
$$
+ \frac{\sin\beta}{V_T}(g\cos\alpha\sin\theta - g\sin\alpha\cos\phi\cos\theta + \frac{T}{m}\cos\alpha)
$$

where $\bar{q} = \frac{1}{2}\rho V_T^2$ and $\rho = 0.001066\ \frac{slugs}{ft^3}$ at an altitude of 25,000 ft.

The equations describing the equations of moment of the aircraft are:

$$
\begin{bmatrix} \dot{p} \\ \dot{q} \\ \dot{r} \end{bmatrix} = \begin{bmatrix} \frac{I_{zz}}{\kappa} & 0 & \frac{I_{xz}}{\kappa} \\ 0 & \frac{1}{I_{yy}} & 0 \\ \frac{I_{xz}}{\kappa} & 0 & \frac{I_{xx}}{\kappa} \end{bmatrix} \left[\left\{ \begin{matrix} L \\ M \\ N \end{matrix} \right\} - \begin{bmatrix} 0 & -r & q \\ r & 0 & -p \\ -q & p & 0 \end{bmatrix} \begin{bmatrix} I_{xx} & 0 & -I_{xz} \\ 0 & I_{yy} & 0 \\ -I_{xz} & 0 & I_{zz} \end{bmatrix} \left\{ \begin{matrix} p \\ q \\ r \end{matrix} \right\} \right]
$$

where $\kappa = I_{xx}I_{zz} - I_{xz}^2$ and L, M, N indicates roll, pitch, and yaw moment:

$$
\begin{bmatrix} L \\ M \\ N \end{bmatrix} = \begin{bmatrix} C_l\bar{q}S_{ref}b_{ref} \\ C_m\bar{q}S_{ref}\bar{c} \\ C_n\bar{q}S_{ref}b_{ref} \end{bmatrix}
$$

The kinematic relations of the aircraft:

$$
\begin{bmatrix} \dot{\phi} \\ \dot{\theta} \\ \dot{\psi} \end{bmatrix} = \begin{bmatrix} 1 & \sin\phi\tan\theta & \cos\phi\tan\theta \\ 0 & \cos\phi & -\sin\phi \\ 0 & \sin\phi\sec\theta & \cos\phi\sec\theta \end{bmatrix} \begin{bmatrix} p \\ q \\ r \end{bmatrix}
$$

2. Full Aerodynamic Model

The aerodynamic coefficients presented here have been extracted from various papers.[13–16] The aerodynamic model of the aircraft is presented and the coefficient values are given in Tables 7, 8.

Pitching Moment, $C_m = C_{m_\alpha}\alpha + C_{m_0} + (C_{m_{\delta_{stab}}}\alpha + C_{m_{\delta_{stab_0}}})\delta_{stab}$

$$+ \frac{\bar{c}}{2V_T}(C_{m_q}\alpha + C_{m_{q_0}})\text{q}$$

Rolling Moment, $C_l = (C_{l_{\beta_2}}\alpha^2 + C_{l_{\beta_1}}\alpha + C_{l_{\beta_0}})\beta + (C_{l_{\delta_{ail}}}\alpha + C_{l_{\delta_{ail_0}}})\delta_{ail}$

$$+ (C_{l_{\delta_{rud}}}\alpha + C_{l_{\delta_{rud_0}}})\delta_{rud} + \frac{b_{ref}}{2V_T}(C_{l_p}\alpha + C_{l_{p_0}})\text{r}$$

Yawing Moment, $C_n = (C_{n_{\beta_2}}\alpha^2 + C_{n_{\beta_1}}\alpha + C_{n_{\beta_0}})\beta + (C_{n_{\delta_{ail}}}\alpha + C_{n_{\delta_{ail_0}}})\delta_{ail}$

$$+ (C_{n_{\delta_{rud}}}\alpha + C_{n_{\delta_{rud_0}}})\delta_{rud} + (C_{n_r}\alpha + C_{n_{r_0}})\frac{b_{ref}}{2V_T}\text{r}$$

<div align="center">

Table 7. Aerodynamic Moment Coefficients

</div>

Pitching Moment			Rolling Moment			Yawing Moment		
C_{m_α}	=	-0.9931	$C_{l_{\beta_2}}$	=	0.8102	$C_{n_{\beta_2}}$	=	-0.3917
C_{m_0}	=	0.1407	$C_{l_{\beta_1}}$	=	-0.6446	$C_{n_{\beta_1}}$	=	0.3648
$C_{m_{\delta_{stab}}}$	=	0.6401	$C_{l_{\beta_0}}$	=	-0.0427	$C_{n_{\beta_0}}$	=	0.0894
$C_{m_{\delta_{stab_0}}}$	=	-1.1055	$C_{l_{\delta_{ail}}}$	=	-0.1553	$C_{n_{\delta_{ail}}}$	=	-0.0213
C_{m_q}	=	-14.30	$C_{l_{\delta_{ail_0}}}$	=	0.1542	$C_{n_{\delta_{ail_0}}}$	=	0.0051
$C_{m_{q_0}}$	=	- 2.00	$C_{l_{\delta_{rud}}}$	=	-0.0858	$C_{n_{\delta_{rud}}}$	=	0.0534
			$C_{l_{\delta_{rud_0}}}$	=	0.0943	$C_{n_{\delta_{rud_0}}}$	=	-0.0724
			C_{l_p}	=	0.0201	C_{n_r}	=	-0.0716
			$C_{l_{p_0}}$	=	-0.3370	$C_{n_{r_0}}$	=	-0.4375

Sideforce Coefficent, $C_Y = (C_{Y_{\beta_2}}\alpha^2 + C_{Y_{\beta_1}}\alpha + C_{Y_{\beta_0}})\beta + (C_{Y_{\delta_{ail}}}\alpha + C_{Y_{\delta_{ail_0}}})\delta_{ail}$

$$+ (C_{Y_{\delta_{rud}}}\alpha + C_{Y_{\delta_{rud_0}}})\delta_{rud}$$

Lift Coefficient, $C_L = (C_{L_{\alpha_3}}\alpha^3 + C_{L_{\alpha_2}}\alpha^2 + C_{L_{\alpha_1}}\alpha + C_{L_{\alpha_0}})\cos(\frac{2\beta}{3})$

$$(C_{L_{\delta_{stab}}}\alpha + C_{L_{\delta_{stab_0}}})\delta_{stab}$$

Drag Coefficient, $C_D = (C_{D_{\alpha_4}}\alpha^4 + C_{D_{\alpha_3}}\alpha^3 + C_{D_{\alpha_2}}\alpha^2 + C_{D_{\alpha_1}}\alpha + C_{D_{\alpha_0}})\cos\beta$

$$+ C_{D_0} + (C_{D_{\delta_{stab}}}\alpha + C_{D_{\delta_{stab_0}}})\delta_{stab}$$

<div align="center">

Table 8. Aerodynamic Force Coefficients

</div>

Sideforce Coefficient			Drag Force Coefficient			Lift Force Coefficient		
$C_{Y_{\beta_2}}$	=	0.5781	$C_{D_{\alpha_4}}$	=	1.4610	$C_{L_{\alpha_3}}$	=	1.1645
$C_{Y_{\beta_1}}$	=	0.2834	$C_{D_{\alpha_3}}$	=	-5.7341	$C_{L_{\alpha_2}}$	=	-5.4246
$C_{Y_{\beta_0}}$	=	-0.8615	$C_{D_{\alpha_2}}$	=	6.3971	$C_{L_{\alpha_1}}$	=	5.6770
$C_{Y_{\delta_{rud}}}$	=	-0.4486	$C_{D_{\alpha_1}}$	=	-0.1995	$C_{L_{\alpha_0}}$	=	-0.0204
$C_{Y_{\delta_{rud_0}}}$	=	0.3079	$C_{D_{\alpha_0}}$	=	-1.4994	$C_{L_{\delta_{stab}}}$	=	-0.3573
$C_{Y_{\delta_{ail}}}$	=	0.4270	C_{D_0}	=	1.5036	$C_{L_{\delta_{stab_0}}}$	=	0.8564
$C_{Y_{\delta_{ail_0}}}$	=	-0.1047	$C_{D_{\delta_{stab}}}$	=	0.7771			
			$C_{D_{\delta_{stab_0}}}$	=	-0.0276			

<div align="center">

American Institute of Aeronautics and Astronautics

</div>

B. Reduced Model

1. Reduced Equations of Motion

Roll-coupled maneuvers[18] of the aircraft are the focus of the analysis. The velocity, V_T, is assumed to be constant and equal to 250 ft/s.

$$\dot{\alpha} = -\frac{\bar{q}S_{ref}}{mV_T}C_L + q - p\beta + \frac{g}{V_T} - r\beta\alpha$$

$$\dot{\beta} = \frac{\bar{q}S_{ref}}{mV_T}(C_D + C_Y\beta) + p\alpha - r + \frac{g}{V_T}\phi$$

$$\dot{p} = \frac{1}{\kappa}(I_{zz}L + I_{xz}N - [I_{xz}^2 + I_{zz}(I_{zz} - I_{yy})]rq)$$

$$\dot{q} = \frac{1}{I_{yy}}(M + (I_{zz} - I_{xx})pr)$$

$$\dot{r} = \frac{1}{\kappa}(I_{xz}L + I_{xx}N + [I_{xz}^2 + I_{xx}(I_{xx} - I_{yy})]pq)$$

$$\dot{\phi} = p$$

2. Reduced Aerodynamic Model

The rolling moment (C_l), pitching moment (C_m), yawing moment (C_n), and sideforce (C_Y) coefficients for the full aerodynamic model presented in Appendix A.2 are same for the reduced aerodynamic model. The lift and drag coefficients have been approximated by employing the standard least square approximation technique within $-20° \leq \beta \leq 20°$, and $-10° \leq \alpha \leq 40°$. The model is presented below:

Lift Coefficient, $C_L := C_{L_{\alpha_2}}\alpha^2 + C_{L_{\alpha_1}}\alpha + C_{L_{\alpha_0}} + (C_{L_{\delta_{stab}}}\alpha + C_{L_{\delta_{stab_0}}})\delta_{stab}$

Drag Coefficient, $C_D := C_{D_{\alpha_2}}\alpha^2 + C_{D_{\alpha_1}}\alpha + C_{D_{\beta_2}}\beta^2 + (C_{D_{\delta_{stab}}}\alpha + C_{D_{\delta_{stab_0}}})\delta_{stab}$

Table 9. Approximated Lift & Drag Force Coefficients

Drag Coefficient			Lift Coefficient		
$C_{D_{\alpha_2}}$	=	2.7663	$C_{L_{\alpha_2}}$	=	−4.5022
$C_{D_{\alpha_1}}$	=	0.1140	$C_{L_{\alpha_1}}$	=	5.4854
$C_{D_{\beta_2}}$	=	1.2838	$C_{L_{\alpha_0}}$	=	−0.0406
$C_{D_{\delta_{stab}}}$	=	0.7771	$C_{L_{\delta_{stab}}}$	=	−0.3573
$C_{D_{\delta_{stab_0}}}$	=	−0.0275	$C_{L_{\delta_{stab_0}}}$	=	0.8563

C. Linearized Model

The reduced order model presented in the Appendix B is used to derive the linearized model around a trim point. The trim values for the states and the inputs are presented in Table 3. The model $\dot{x}_{OL} = Ax_{OL} + Bu$ with the output equation $y = Cx_{OL} + Du$ is presented in this section. The ordering of the states, inputs and outputs are mentioned below: $x_{OL}^{T} = [\beta \quad p \quad r \quad \phi \quad \alpha \quad q \ ]$ and $u = [\delta_{ail} \quad \delta_{rud} \quad \delta_{stab} \quad T]$. However, the C and D matrices will be different for each of the control law due to different feedback measurements. They are: $y_{Baseline}^{T} = [a_y \quad p \quad r \quad \alpha \quad q]$ and $y_{Revised}^{T} = [a_y \quad p \quad r \quad \alpha \quad \beta \quad q \quad \dot{\beta}]$

The open loop plant, G , is represented as: $G = \left[\begin{array}{c|c} A & B \\ \hline C_{Revised} & D_{Revised} \end{array}\right]$ The linearized matrices for 60° bank angle turn (Plant 4 in Table 3) is presented. The C and D matrices will be presented for the revised flight control law. Appropriate C and D matrices for the baseline flight control law can be extracted from these matrices.

$$
\left[\begin{array}{c|c} A & B \end{array}\right] =
\left[\begin{array}{cccccc|cccc}
-0.0059 & 0.4538 & -1 & 0.1288 & 0.0026 & 0 & 0.0046 & 0.0054 & 0 & 0 \\
-3.6680 & -0.4000 & 0.0134 & 0 & -0.0015 & -0.1095 & 1.8210 & 0.2573 & 0 & 0 \\
0.1382 & 0.0070 & -0.1034 & 0 & -0.0184 & 0 & -0.0453 & -0.1459 & 0 & 0 \\
0 & 1 & 0 & 0 & 0 & 0 & 0 & 0 & 0 & 0 \\
-0.0609 & 0 & 0 & 0 & -0.2201 & 1 & 0 & 0 & -0.0358 & -1.755 \times 10^{-6} \\
0 & 0.1305 & 0 & 0 & -1.2550 & -0.1984 & 0 & 0 & -0.8269 & 0
\end{array}\right]
$$

The C and D matrices for the revised controller are as follows:

$$
\left[\begin{array}{c|c} C_{Revised} & D_{Revised} \end{array}\right] =
\left[\begin{array}{cccccc|cccc}
-0.2456 & 0 & 0 & 0 & 0.02005 & 0 & 0.0356 & 0.0418 & 0 & 0 \\
0 & 1 & 0 & 0 & 0 & 0 & 0 & 0 & 0 & 0 \\
0 & 0 & 1 & 0 & 0 & 0 & 0 & 0 & 0 & 0 \\
0 & 0 & 0 & 0 & 1 & 0 & 0 & 0 & 0 & 0 \\
0 & 0 & 0 & 0 & 0 & 1 & 0 & 0 & 0 & 0 \\
0 & 0.4538 & -1 & 0.1288 & 0 & 0 & 0 & 0 & 0 & 0
\end{array}\right]
$$

D. Control Law State Space Realization

The state space realization of both the baseline and the revised control laws are presented here. The controller, $K = \left[\begin{array}{c|c} A_c & B_c \\ \hline C_c & D_C \end{array}\right]$ where $\dot{x}_c = A_c x_c + B_c y$ and $u = C_c x_c + D_c y$ describes the controllers' state space realization with u and y as described in Appendix C.

1. *Baseline Controller Realization:* $y = y_{Baseline}$

$$
\left[\begin{array}{c|c} A_c & B_c \\ \hline C_c & D_c \end{array}\right] =
\left[\begin{array}{c|ccccc}
-1 & 0 & 0 & 4.9 & 0 & 0 \\
\hline
0 & 0 & 0.8 & 0 & 0 & 0 \\
-1 & -0.5 & 0 & -1.1 & 0 & 0 \\
0 & 0 & 0 & 0 & -0.8 & -8 \\
0 & 0 & 0 & 0 & 0 & 0
\end{array}\right]
$$

2. *Revised Controller Realization:* $y = y_{Revised}$

$$
\left[\begin{array}{c|c} A_c & B_c \\ \hline C_c & D_c \end{array}\right] =
\left[\begin{array}{c|ccccccc}
-1 & 0 & 0 & 4.9 & 0 & 0 & 0 & 0 \\
\hline
0 & 0 & 0.8 & 0 & 0 & 2 & 0 & 0.5 \\
-1 & -0.5 & 0 & -1.1 & 0 & 0 & 0 & 0 \\
0 & 0 & 0 & 0 & -0.8 & 0 & -8 & 0 \\
0 & 0 & 0 & 0 & 0 & 0 & 0 & 0
\end{array}\right]
$$

American Institute of Aeronautics and Astronautics

E. Third Order Approximated Polynomial Closed-Loop Models

1. Baseline Controller Closed-Loop Model

$$\dot{\beta} = 0.20127\alpha^2\beta - 0.0015591\alpha^2\mathrm{p} - 0.0021718\alpha^2\mathrm{r} + 0.0019743\alpha^2 x_c + 0.32034\alpha\beta\mathrm{q} + 0.065962\beta^3$$
$$+ 0.17968\alpha\beta + 0.98314\alpha\mathrm{p} - 0.023426\alpha\mathrm{r} - 0.024926\alpha x_c + 0.134\beta\mathrm{q} + 0.0025822\alpha - 0.0068553\beta$$
$$+ 0.45003\mathrm{p} + 0.1288\phi - 0.99443\mathrm{r} + 0.0056922 x_c$$

$$\dot{\mathrm{p}} = 17.7160\alpha^2\beta - 0.0277\alpha^2\mathrm{p} - 0.0386\alpha^2\mathrm{r} + 0.0351\alpha^2 x_c - 0.0033\beta^3 + 2.1835\alpha\beta + 3.0420\alpha\mathrm{p}$$
$$- 0.4139\alpha\mathrm{r} - 0.4699\alpha x_c - 0.8151\mathrm{qr} - 0.0015\alpha - 3.7098\beta - 1.8607\mathrm{p} - 0.1096\mathrm{q} + 0.2799\mathrm{r}$$
$$+ 0.2723 x_c$$

$$\dot{\mathrm{r}} = -1.4509\alpha^2\beta + 0.0105\alpha^2\mathrm{p} + 0.0146\alpha^2\mathrm{r} - 0.0133\alpha^2 x_c + 0.0012\beta^3 - 1.0095\alpha\beta - 0.0148\alpha\mathrm{p}$$
$$+ 0.1410\alpha\mathrm{r} + 0.1854\alpha x_c - 0.7544\mathrm{pq} - 0.0185\alpha + 0.1620\beta + 0.0455\mathrm{p} - 0.2546\mathrm{r} - 0.1544 x_c$$

$$\dot{\phi} = \mathrm{p}$$

$$\dot{\alpha} = -\alpha\beta\mathrm{r} + 0.2467\alpha^2 - 0.1344\alpha\beta + 0.1473\alpha\mathrm{q} - \beta\mathrm{p} - 0.4538\beta\mathrm{r} - 0.2487\alpha - 0.0609\beta + 0.7139\mathrm{q}$$

$$\dot{\mathrm{q}} = 0.5196\alpha^2 + 4.8613\alpha\mathrm{q} + 0.97126\mathrm{pr} - 1.9162\alpha - 6.8140\mathrm{q} + 0.1305\mathrm{p}$$

$$\dot{x_c} = 4.9\mathrm{r} - x_c$$

2. Revised Controller Closed-Loop Model

$$\dot{\beta} = 0.1831\alpha^2\beta - 0.0496\alpha^2\mathrm{p} - 0.0005\alpha^2\phi + 0.0017\alpha^2\mathrm{r} + 0.0030\alpha^2 x_c + 0.3203\alpha\beta\mathrm{q} + 0.0643\beta^3$$
$$+ 0.0027\alpha\beta + 0.9557\alpha\mathrm{p} - 0.0054\alpha\phi + 0.0187\alpha\mathrm{r} - 0.0250\alpha x_c + 0.1340\beta\mathrm{q} + 0.0026\alpha - 0.0091\beta$$
$$+ 0.4457\mathrm{p} + 0.1276\phi - 0.9850\mathrm{r} + 0.0056 x_c$$

$$\dot{\mathrm{p}} = 1.1530\alpha^2\beta + 6.6577\alpha^2\mathrm{p} - 0.0082\alpha^2\phi + 0.0308\alpha^2\mathrm{r} - 0.1205\alpha^2 x_c + 18.3689\beta^3 - 0.5080\alpha\beta$$
$$+ 2.4908\alpha\mathrm{p} + 0.8743\alpha\phi - 7.2037\alpha\mathrm{r} - 0.3495\alpha x_c - 0.8151\mathrm{qr} - 0.0109\alpha - 4.6009\beta$$
$$- 3.5186\mathrm{p} - 0.4703\phi - 0.1096\mathrm{q} + 3.9316\mathrm{r} + 0.2527 x_c$$

$$\dot{\mathrm{r}} = -1.4275\alpha^2\beta + 0.0546\alpha^2\mathrm{p} + 0.0031\alpha^2\phi - 0.0117\alpha^2\mathrm{r} - 0.0132\alpha^2 x_c + 0.0079\beta^3 - 1.0008\alpha\beta$$
$$- 0.0096\alpha\mathrm{p} - 0.0029\alpha\phi + 0.1638\alpha\mathrm{r} + 0.1832\alpha x_c - 0.7544\mathrm{pq} - 0.0182\alpha + 0.1854\beta + 0.0895\mathrm{p}$$
$$+ 0.0124\phi - 0.3509\mathrm{r} - 0.1539 x_c$$

$$\dot{\phi} = \mathrm{p}$$

$$\dot{\alpha} = -\alpha\beta\mathrm{r} + 0.2467\alpha^2 - 0.1344\alpha\beta + 0.1473\alpha\mathrm{q} - \beta\mathrm{p} - 0.4538\beta\mathrm{r} - 0.2487\alpha - 0.0609\beta + 0.7139\mathrm{q}$$

$$\dot{\mathrm{q}} = 0.5196\alpha^2 + 4.8613\alpha\mathrm{q} + 0.97126\mathrm{pr} - 1.9162\alpha - 6.8140\mathrm{q} + 0.1305\mathrm{p}$$

$$\dot{x_c} = 4.9\mathrm{r} - x_c$$

References

[1] Heller, M., David, R., and Holmberg, J., "Falling leaf motion suppression in the F/A-18 Hornet with revised flight control software," *AIAA Aerospace Sciences Meeting*, No. AIAA-2004-542, 2004.

[2] Topcu, U., Packard, A., Seiler, P., and Wheeler, T., "Stability region analysis using simulations and sum-of-squares programming," *Proceedings of the American Control Conference*, 2007, pp. 6009–6014.

[3] Topcu, U., Packard, A., and Seiler, P., "Local stability analysis using simulations and sum-of-Squares programming," *Automatica*, Vol. 44, No. 10, 2008, pp. 2669–2675.

[4] Tan, W., *Nonlinear Control Analysis and Synthesis using Sum-of-Squares Programming*, Ph.D. thesis, University of California, Berkeley, 2006.

[5] Parrilo, P., *Structured Semidefinite Programs and Semialgebraic Geometry Methods in Robustness and Optimization*, Ph.D. thesis, California Institute of Technology, 2000.

[6] Prajna, S., Papachristodoulou, A., Seiler, P., and Parrilo, P. A., *SOSTOOLS: Sum of squares optimization toolbox for MATLAB*, 2004.

[7] Jaramillo, P. T. and Ralston, J. N., "Simulation of the F/A-18D falling leaf," *AIAA Atmospheric Flight Mechanics Conference*, 1996, pp. 756–766.

⁸Buttrill, S. B., Arbuckle, P. D., and Hoffler, K. D., "Simulation model of a twin-tail, high performance airplane," Tech. Rep. NASA TM-107601, NASA, 1992.

⁹Stengel, R., *Flight Dynamics*, Princeton University Press, 2004.

¹⁰Cook, M., *Flight Dynamics Principles*, Wiley, 1997.

¹¹Napolitano, M. R. and Spagnuolo, J. M., "Determination of the stability and control derivatives of the NASA F/A-18 HARV using flight data," Tech. Rep. NASA CR-194838, NASA, 1993.

¹²Stevens, B. and Lewis, F., *Aircraft Control and Simulaion*, John Wiley & Sons, 1992.

¹³Napolitano, M. R., Paris, A. C., and Seanor, B. A., "Estimation of the lateral-directional aerodynamic parameters from flight data for the NASA F/A-18 HARV," *AIAA Atmospheric Flight Mechanics Conference*, No. AIAA-96-3420-CP, 1996, pp. 479–489.

¹⁴Lluch, C. D., *Analysis of the Out-of-Control Falling Leaf Motion using a Rotational Axis Coordinate System*, Master's thesis, Virginia Polytechnic Institue and State Unniversity, 1998.

¹⁵Napolitano, M. R., Paris, A. C., and Seanor, B. A., "Estimation of the longitudinal aerodynamic parameters from flight data for the NASA F/A-18 HARV," *AIAA Atmospheric Flight Mechanics Conference*, No. AIAA-96-3419-CP, pp. 469–478.

¹⁶Iliff, K. W. and Wang, K.-S. C., "Extraction of lateral-directional stability and control derivatives for the basic F-18 aircraft at high angles of attack," *NASA TM-4786*, 1997.

¹⁷Illif, K. W. and Wang, K.-S. C., "Retrospective and recent examples of aircraft parameter identification at NASA Dryden Flight Research Center," *Journal of Aircraft*, Vol. 41, No. 4, 2004.

¹⁸Schy, A. and Hannah, M. E., "Prediction of jump phenomena in roll-coupled maneuvers of airplanes," *Journal of Aircraft*, Vol. 14, No. 4, 1977, pp. 375– 382.

¹⁹Heller, M., Niewoehner, R., and Lawson, P. K., "High angle of attack control law development and testing for the F/A-18E/F Super Hornet," *AIAA Guidance, Navigation, and Control Conference*, No. AIAA-1999-4051, 1999, pp. 541–551.

²⁰Balas, G., Chiang, R., Packard, A., and Safonov, M., *Robust Control Toolbox*, MathWorks, 2008.

²¹Heller, M., Niewoehner, R., and Lawson, P. K., "On the Validation of Safety Critical Aircraft Systems, Part I: An Overview of Analytical & Simulation Methods," *AIAA Guidance, Navigation, and Control Conference*, No. AIAA 2003-5559, 2003.

²²Khalil, H., *Nonlinear Systems*, Prentice Hall, 2nd ed., 1996.

²³Vidyasagar, M., *Nonlinear Systems Analysis*, Prentice Hall, 2nd ed., 1993.

²⁴Vannelli, A. and Vidyasagar, M., "Maximal Lyapunov functions and domains of attraction for autonomous nonlinear systems," *Automatica*, Vol. 21, No. 1, 1985, pp. 69–80.

²⁵Tibken, B. and Fan, Y., "Computing the domain of attraction for polynomial systems via BMI optimization methods," *Proceedings of the American Control Conference*, 2006, pp. 117–122.

²⁶Tibken, B., "Estimation of the domain of attraction for polynomial systems via LMIs," *Proceedings of the IEEE Conference on Decision and Control*, 2000, pp. 3860–3864.

²⁷Hauser, J. and Lai, M., "Estimating quadratic stability domains by nonsmooth optimization," *Proceedings of the American Control Conference*, 1992, pp. 571–576.

²⁸Hachicho, O. and Tibken, B., "Estimating domains of attraction of a class of nonlinear dynamical systems with LMI methods based on the theory of moments," *Proceedings of the IEEE Conference on Decision and Control*, 2002, pp. 3150–3155.

²⁹Genesio, R., Tartaglia, M., and Vicino, A., "On the estimation of asymptotic stability regions: State of the art and new proposals," *IEEE Transactions on Automatic Control*, Vol. 30, No. 8, 1985, pp. 747–755.

³⁰Davison, E. and Kurak, E., "A computational method for determining quadratic Lyapunov functions for nonlinear systems," *Automatica*, Vol. 7, 1971, pp. 627–636.

³¹Chiang, H.-D. and Thorp, J., "Stability regions of nonlinear dynamical systems: A constructive methodology," *IEEE Transactions on Automatic Control*, Vol. 34, No. 12, 1989, pp. 1229–1241.

³²Jarvis-Wloszek, Z., *Lyapunov Based Analysis and Controller Synthesis for Polynomial Systems using Sum-of-Squares Optimization*, Ph.D. thesis, University of California, Berkeley, 2003.

³³Jarvis-Wloszek, Z., Feeley, R., Tan, W., Sun, K., and Packard, A., "Some Controls Applications of Sum of Squares Programming," *Proceedings of the 42nd IEEE Conference on Decision and Control*, Vol. 5, 2003, pp. 4676–4681.

³⁴Tan, W. and Packard, A., "Searching for control Lyapunov functions using sums of squares programming," *42nd Annual Allerton Conference on Communications, Control and Computing*, 2004, pp. 210–219.

³⁵Jarvis-Wloszek, Z., Feeley, R., Tan, W., Sun, K., and Packard, A., *Positive Polynomials in Control*, Vol. 312 of *Lecture Notes in Control and Information Sciences*, chap. Controls Applications of Sum of Squares Programming, Springer-Verlag, 2005, pp. 3–22.

³⁶Lofberg, J., "YALMIP : A Toolbox for Modeling and Optimization in MATLAB," *Proceedings of the CACSD Conference*, Taipei, Taiwan, 2004.

³⁷Sturm, J., "Using SeDuMi 1.02, a MATLAB toolbox for optimization over symmetric cones," *Optimization Methods and Software*, 1999, pp. 625–653.